

Geometry-based Discovery of Calcium Battery Cathodes Accelerated by Foundational Machine-Learned Models

Dereje Bekele Tekliye¹, Achintha Krishna Bheemaguli¹, and Gopalakrishnan Sai
Gautam^{1,*}

¹Department of Materials Engineering, Indian Institute of Science, Bengaluru, 560012,
India

*Email: saigautamg@iisc.ac.in

Abstract

Calcium batteries (CBs) are an attractive post-Li-ion technology, offering the appeal of Ca’s natural abundance, redox potential close to Li, and high volumetric energy density. However, practical realization of CBs remains limited by the scarcity of positive electrode (cathode) materials that support reversible Ca^{2+} (de)intercalation under typical electrochemical conditions. To address this challenge, we screen the materials project (MP) database for novel host structures that can intercalate Ca using geometry- and chemistry-based design principles. Specifically, we employ the Voronoi polyhedral volume as a descriptor of site compatibility for hosting Ca in potential frameworks. Further, we down-select candidate structures progressively through diverse criteria including charge neutrality, absence of non-Ca mobile cations, thermodynamic (meta)stability, average voltage, and Ca migration barriers (E_m) using foundational machine-learning (ML) models. Subsequently, we validate the ML-predicted E_m , obtained via an ensemble prediction among three distinct ML models, in a subset of the final candidates using density functional theory based nudged elastic band calculations. Overall, from an initial pool of 52,945 MP structures, our high-throughput workflow identifies 37 promising Ca cathode candidates, several of which exhibit favorable combinations of thermodynamic (meta)stability, voltage, and Ca^{2+} mobility, marking them as strong candidates for experimental synthesis and electrochemical characterization. Particularly, we identify two Ca cathode candidates with markedly low Ca^{2+} E_m , including $\text{CaSc}_2\text{V}_2\text{O}_8$ (213 meV) and CaVSO_4F_3 (376 meV), and four cathode candidates ($\text{Ca}_3(\text{CoO}_2)_4$, $\text{Ca}_3\text{Mn}_4(\text{TeO}_6)_2$, CaVF_5 , and CaVSO_4F_3) with thermodynamic stability in their charged composition. Beyond identifying Ca-cathodes, our work establishes geometry-based descriptors and ML-based workflows as transferable methods for high-throughput screening, enabling the rational discovery of novel materials for battery and other applications.

1 Introduction

Lithium-ion batteries (LIBs) are the workhorse of modern energy storage, powering everything from portable electronics to electric vehicles and grid systems. [1–4] The high energy density, long cycle life, and rapidly declining costs of LIBs have enabled their widespread deployment at scale. [5, 6] Nevertheless, rising demand for energy storage, supply-chain constraints, safety considerations, and performance bottlenecks continue to

motivate the search for next-generation electrode materials and chemistries. [7,8] In this context, multivalent battery systems, such as those based on Mg, Ca, Zn, or Al, offer significant promise because multi-electron redox and the possibility of using a metallic anode can facilitate higher volumetric energy density compared to LIBs. [9–14] Among multivalent systems, Ca is particularly attractive due to *i*) its redox potential being close to that of Li (-2.87 V vs. SHE), *ii*) Ca metal anode enabling high volumetric energy densities (theoretical capacity of 1337 mAh g^{-1} and 2073 Ah L^{-1}), and *iii*) Ca’s availability on the earth’s crust as the fifth most abundant element. [9, 15–21] Thus, development of reversible battery systems based on Ca as the electroactive ion retain a lot of promise as an alternative to LIBs.

Recent advances in the design of Ca electrolytes have enabled reversible Ca plating and stripping at or near room temperature, markedly improving practical feasibility of a Ca-battery (CB). [22–24] Yet, the positive electrode (cathode) remains the critical bottleneck for the development of a practical Ca-battery. Unlike monovalent Li^+ , divalent Ca^{2+} exhibits poor diffusion in most inorganic frameworks due to its large ionic radius (~ 1 Å in an octahedral coordination environment surrounded by O^{2-}) and high electrostatic charge, which require ‘wide’ diffusion pathways. Consequently, many candidate hosts exhibit high migration barriers (E_m), [25–29] structural instabilities at operating voltages, and/or undesirable reactivity with the electrolyte. [30] The central challenge, therefore, is to identify cathode frameworks that simultaneously deliver low Ca^{2+} E_m , thermodynamic and interfacial stability, and practical voltages, while remaining synthesizable and chemically robust under realistic battery conditions.

Extensive experimental and computational efforts have been devoted to exploring potential Ca-battery cathodes across various crystal frameworks, including tunnel, layered, and spinel oxides, [19, 27, 28, 31–43] Chevrel-type sulfides, [44] Prussian blue analogues, [45–49] polyanionic hosts such as phosphates, and sodium superionic conductor (NaSICON) structures, [50–54] and fluorides. [55] For example, a high-throughput density functional theory (DFT [56, 57]) study by Lu *et al.* identified post-spinel CaV_2O_4 and layered CaNb_2O_4 as promising compositions based on intercalation voltage, thermodynamic stability, and E_m criteria, with early experiments indicating potential yet still requiring framework optimization. [35] A recent work on post-spinel CaMn_2O_4 phase showed limited cycling performance (52 mAh g^{-1} at $C/33$), [27] while a water-free $\beta\text{-Ca}_{0.14}\text{V}_2\text{O}_5$ delivered a reversible capacity of ~ 247 mAh g^{-1} with improved cycling stability and minimal dimensional change compared to hydrated and layered V_2O_5 phases. [33]

Among polyanionic frameworks, FePO_4 accommodates ~ 0.2 mol of Ca^{2+} at 2.9 V with some reversibility. [51] Fluorinated vanadium phosphate, $\text{Na}_{0.5}\text{VPO}_{4.8}\text{F}_{0.7}$, exhibits excellent Ca cycling stability, retaining 90% of its capacity after 500 cycles with a capacity near 87 mAh g^{-1} . [53] A recent experimental and computational study on $\text{Ca}_x\text{NaV}_2(\text{PO}_4)_3$ revealed a reversible Ca content limited to $x \approx 0.65$, associated with phase separation into Na-rich and Ca-rich domains. [58] Notably, presence of Na within the framework is attributed to facilitate neighboring Ca^{2+} migration, thus promoting reversible electrochemical activity, a recurring feature in studies involving polyanionic frameworks as Ca-cathodes.

Additionally, given the similar ionic radii of Ca^{2+} and Na^+ , structural frameworks that accommodate reversible Na intercalation are potential hosts for Ca insertion as well. [59, 60] Indeed, experimental studies on NaSICON-type $\text{NaV}_2(\text{PO}_4)_3$ have demonstrated reversible Ca intercalation, up to 0.6 mol Ca^{2+} at 3.2 V vs. Ca, [51] indicating that NaSICON frameworks can serve as hosts for Ca-cathodes, thereby motivating our prior extensive DFT-based screening of NaSICON and fluoride chemistries as Ca-cathodes. [54, 55, 61] Specifically, we evaluated the average Ca-intercalation voltage, 0 K thermodynamic stability of intercalated (or discharged) and deintercalated (charged) compositions, and Ca^{2+} E_m within the NaSICON polyanionic family, $\text{Ca}_x\text{M}_2(\text{ZO}_4)_3$ with $Z = \text{Si, P, or S}$ and $M = \text{Ti, V, Cr, Mn, Fe, Co, or Ni}$. [54] Subsequently,

we identified $\text{Ca}_x\text{V}_2(\text{PO}_4)_3$, $\text{Ca}_x\text{Mn}_2(\text{SO}_4)_3$, and $\text{Ca}_x\text{Fe}_2(\text{SO}_4)_3$ as promising Ca-cathode candidates, while silicate NaSICONs were predicted to be unstable, with experimental realization of the Mn- and Fe-NaSICON candidates still pending. [54]

We extended our exploration to transition metal (TM) fluorides, including weberite- $\text{Ca}_x\text{M}_2\text{F}_7$ and perovskite- Ca_xMF_3 compositions, using the same suite of 3d TMs and computing similar metrics as the NaSICON study. [55] Importantly, we identified weberite- $\text{Ca}_x\text{Cr}_2\text{F}_7$ and weberite- $\text{Ca}_x\text{Mn}_2\text{F}_7$ as promising Ca-cathodes. Note that the design principle of cation substitution being largely governed by size compatibility can be generalized further by quantifying the similarity in ionic sizes via estimation of the Voronoi polyhedral volume (VPV [62]). Unlike tabulated ionic radii, VPV captures the true local coordination environment that can accommodate a given cation, and better captures similarities across multiple combinations of structures, chemistries, and ions of interest, enabling physically-grounded identification of compatible host sites across diverse structures. We utilize the VPV metric in identifying novel Ca-cathodes in this work.

In general, DFT-based high-throughput explorations are well suited for materials discovery and design, such as the identification of potential Ca-cathodes. However, the computational costs associated with such high-throughput studies scale rapidly with increasing the chemical or structural space and the number of properties that are used during the screening process. Recent advances in machine-learned interatomic potentials (MLIPs), resulting in ‘foundational’ or ‘universal’ potentials, have transformed materials modeling by combining near quantum-mechanical accuracy with broad scalability and lower computational costs, enabling high-throughput and multiscale simulations. [63–70] Among the available MLIPs, the multi atomic cluster expansion (MACE [63,64]) framework has emerged as a particularly promising approach as it is built on high body-order equivariant message-passing graph neural networks. Batatia et al. [63,68] introduced pre-trained MACE-MP-0 foundation models, namely, small, medium, and large, that differ in the degree of equivariance during message passing, i.e., $L_{\max} = 0, 1, \text{ and } 2$, respectively. The MACE-MP-0 models are trained on the materials project (MP [71]) trajectory (or MPtrj [72]) dataset covering 89 elements, which enable accurate and transferable modeling of atomic interactions across diverse material systems. Thus, the development of MACE-MP-0, and other universal potentials, have accelerated materials discovery across a wide range of applications, including batteries, [73–76] catalysis, [77] photovoltaics, [78,79] semiconductors, [80] and structural systems, [81] [82] by providing a pathway to sample across more extensive chemical and structural spaces efficiently. [83,84]

Here, we integrate a geometry-based design strategy with a MLIP-accelerated high-throughput workflow to move beyond framework-by-framework evaluation and systematically identify previously unexplored chemistries and structures that can host Ca and function as cathodes for Ca-batteries. We examine available frameworks in the MP, a database of DFT-calculated properties largely based on structures from the inorganic crystal structure database, [85] with a focus on identifying novel non-Ca-containing structures that can host Ca. We use the MACE-MP-0 large foundational model for rapid geometry optimization, accelerating the evaluation of the ground-state Ca-configuration and the associated total energy, and aiding the estimation of Ca E_m to identify potential candidates. Note that E_m predictions by a single foundational MLIP may not be as accurate across a wide range of chemistries and E_m values, as suggested by a recent benchmarking study. [76] Thus, in addition to MACE-MP-0, we employ another foundational MLIP, namely Orb-v3, [70] and a graph-based transfer-learned (TL) property predictor model [86–88] to increase the confidence in E_m predictions and identify candidates with higher precision. The three machine-learned (ML) models operate in a ‘mixture-of-experts’ (MoE) or an ‘ensemble’ combination, thereby boosting the accuracy in E_m predictions.

Overall, starting from 52,945 inorganic compounds, we apply chemically-motivated filters, including the geometric Ca-VPV tolerance, charge neutrality, thermodynamic stability (at 0 K), average Ca-intercalation voltage, and $\text{Ca}^{2+} E_m$, and arrive at a set of 37 promising frameworks as Ca-intercalating cathodes. Further, we validate our MoE-predicted $\text{Ca}^{2+} E_m$ values with DFT-based nudged elastic band (NEB [89, 90]) calculations, with all converged results falling within our predefined tolerance, confirming the reliability of the ensemble-guided screening. Importantly, we identify two cathode candidates that display exceptionally low DFT-NEB-calculated $\text{Ca}^{2+} E_m$, namely $\text{CaSc}_2\text{V}_2\text{O}_8$ (213 meV) and CaVSO_4F_3 (376 meV), besides highlighting $\text{Ca}_3(\text{CoO}_2)_4$, $\text{Ca}_3\text{Mn}_4(\text{TeO}_6)_2$, CaVF_5 , and CaVSO_4F_3 as promising due to their thermodynamic stability at the charged composition. Our unified high-throughput ML-accelerated discovery framework delivers orders-of-magnitude acceleration in materials discovery while maintaining the fidelity required for experimental down-selection. To our knowledge, our study is the largest-scale exploration of possible Ca-cathode chemical space, so far, and our high-throughput workflow is readily transferable for identifying novel materials for other battery chemistries and other applications.

2 Methods

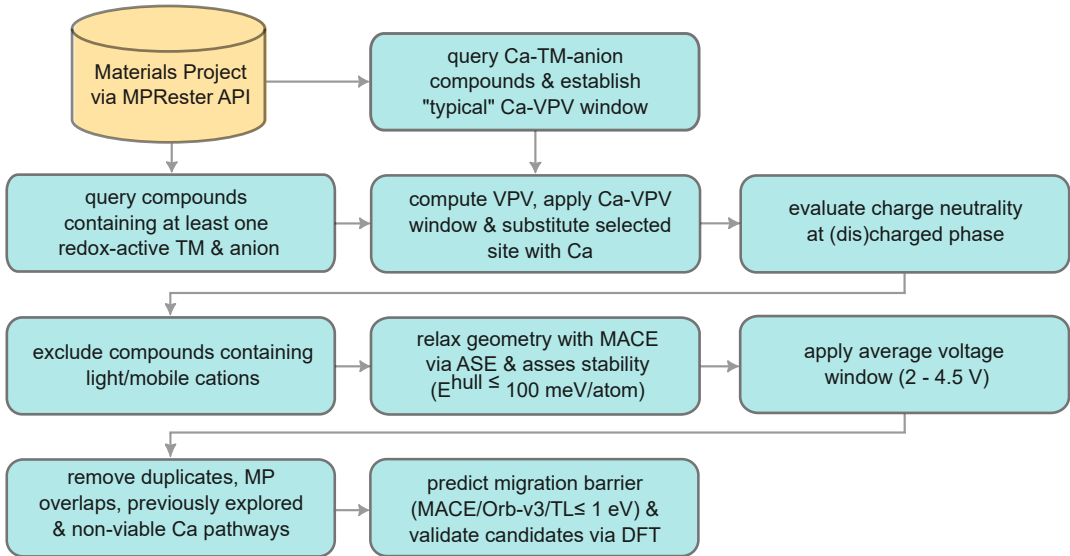


Figure 1: Schematic overview of the high-throughput ML-accelerated screening workflow developed in this work for identifying promising Ca-intercalation cathode frameworks.

2.1 VPV-based framework screening

Figure 1 summarizes the screening workflow used in this study. We began by querying Ca-containing compounds that include at least one TM (not necessarily redox-active) and one anion from the MP database (as available on May 7, 2025), using the MPRester API in pymatgen. [91] We refer to the collection of all queried compounds, amounting to 4,350 frameworks, as ‘set 1’ and considered compounds regardless of whether they have been previously studied for battery applications. Subsequently, we used the retrieved structures to estimate the ‘typical’ polyhedral volumes that Ca^{2+} occupies in Ca-containing structures,

based on the VPV metric. We computed the Ca VPV in a given structure with `pymatgen`'s `VoronoiNN` class by constructing the Voronoi tessellation around all Ca sites and averaging the corresponding polyhedral volumes. The VPV calculation is done to establish a representative Ca-VPV window, i.e., the typical range of polyhedral volumes that Ca prefers among inorganic structures, centered around the median VPV value with a $\pm 5\%$ tolerance across all queried compounds that contain Ca. This VPV range was then used to quantify geometric compatibility of lattice (or void) sites that can possibly accommodate Ca and hence identify potential Ca sites within structures that do not contain Ca *a priori*.

Upon obtaining the typical Ca VPV, we queried the MP database by explicitly excluding Ca-containing entries and including at least one redox-active TM (Ti, V, Cr, Mn, Fe, Co, Ni, Nb, and/or Mo), and at least one anion (O, S, Se, Te, N, P, F, Cl, Br, and/or I) to identify novel cathodes that do not contain Ca *a priori*, forming our 'set 2' containing 52,945 compounds. The list of redox-active TMs, the corresponding allowed oxidation states of TMs, and anions considered is compiled in **Table S1** of the supporting information (SI). Any cation species other than the 'framework-forming' elements (i.e., the redox-active TM and anions) were considered for potential substitution with Ca, subject to their compatibility with the VPV metric, along with possible interstitial/vacancy sites in the structure. If no species other than the redox-active TM and anions were present in a structure, we assessed possible interstitial/vacancy sites available in the structure for Ca insertion. To identify potential vacancy/interstitial sites in a given structure, we used `pymatgen`'s `TopographyAnalyzer`. We required any candidate vacancy/interstitial site to have a minimum distance of 1 Å to the nearest framework atom. If multiple sites that are closer than 1 Å from one another are identified, we retained only a single representative site among them. Upon identification of a suitable site, we placed a dummy chemical species ('X') and calculated the VPV for that site.

Finally, we used the established Ca-VPV tolerance window to estimate the geometric compatibility of possible substitution and/or vacancy/interstitial sites across all non-Ca-containing queried compounds of set 2. If a structure contained both substitutional and X sites that can be occupied by Ca, we considered the possibility of Ca occupying the substitutional site only. Thus, X sites are considered in the absence of any possible substitutional sites that Ca can occupy in a framework. If multiple sites in a structure fell within the VPV tolerance window, we selected the site with a VPV value closest to the Ca-VPV median for Ca substitution/insertion. In the event of a tie, we chose a site at random. Note that we did not down-select any structures from set 1 that contain redox-active TMs and are within the target Ca-VPV window since such structures may have been considered already in previous screening studies. [35] Thus, our final list of geometry-compatible compounds contain frameworks from set 2 that fall within the Ca-VPV window, with possible Ca substitution at existing cation sites or Ca insertion in X sites. The queried list of compounds (i.e., MP-IDs of structures) comprising our sets 1 and 2 are available in our GitHub repository.

2.2 Charge neutrality constraint

Charge neutrality is one of the prerequisites for thermodynamic stability and, by extension, for chemical synthesizability. As cathode compositions evolve during electrochemical cycling, we require that each composition encountered remain electrostatically neutral. We therefore evaluate the two end members, namely, the fully 'discharged' state containing the maximum possible occupation of Ca and the fully 'charged' state with the minimum possible occupation of Ca. For both end member compositions, we constrain the sum of ionic charges, as determined via allowed oxidation states for different species present (see **Table S1**), to be zero. We assigned oxidation states using `pymatgen`'s `Composition` class, following chemical constraints on possible oxidation states (see Section S1 of SI). [92] For instance, we limit the oxidation states of redox-active

TMs to be in the range of +2 to +4 (except V which is allowed between +2 and +5) and allowed fractional TM oxidation states (e.g., 3.5+) to account for mixed-valence. On the other hand, we allowed either a single or a small set of integer oxidation states for p -block elements. Among the queried structures, we did not encounter cases where both positive and negative oxidation states had to be assigned for the same element (e.g., both +6 and -2 for S in the same structure). When multiple p -block elements are present, we constrained the oxidation state of the most electronegative element to be in its lowest negative state (e.g., -2 for O). While our oxidation state constraints are not exhaustive, they do eliminate most charge-imbalanced compositions, with any remaining cases removed by subsequent thermodynamic evaluation (see Section 2.4).

2.3 Mobile-cation-containing compound exclusion

Several cations, including H, Li, Na, K, Mg, and Zn, are known to be mobile in solid-state materials, particularly cathode compositions. [10, 93–95] In structures that contain both Ca and an additional mobile cation, such as Li, the electrochemical behavior can arise from the motion of Ca and/or Li. Therefore, to ensure that Ca serves as the sole electroactive ion in a candidate cathode material, all Ca-cathode candidates that satisfy the charge-neutrality constraint but contain additional mobile cations (as mentioned above) were excluded from the dataset. The remaining charge-neutral candidates that contain only Ca as the electroactive species are evaluated subsequently.

2.4 Thermodynamic stability and average voltage

To evaluate thermodynamic stability with respect to other competing phases, we use the MACE-MP-0 large foundational model, hereafter referred to simply as MACE. Specifically, we performed MACE-based geometry relaxations for the selected candidates following Sections 2.2 and 2.3, in both their charged and discharged compositions. We employed the atomistic simulation environment (ASE [96]) for structural optimization, using the MACE calculator for estimating total energies and atomic forces. ASE’s `UnitCellFilter` was used to allow simultaneous relaxation of both atomic positions and cell vectors, via the `QuasiNewton` optimizer. We considered a structural optimization converged when the interatomic forces were below $|0.05|$ eV/Å over a maximum of 1,000 optimization steps.

Because the MACE model used in this work is trained on uncorrected MP energies, we applied the `MaterialsProject2020Compatibility` [97,98] correction scheme in `pymatgen` to our MACE-calculated energies to maintain consistency with the data available on MP. Specifically, we used the corrected MP energies of all possible competing phases, as available on MP, for constructing the corresponding 0 K convex hulls and assessing the thermodynamic stability for both charged and discharged compositions. Notably, we computed the energy above the convex hull (E^{hull}) for each Ca-based compound. Given typical DFT errors in 0 K stability predictions [99] and residual MACE-to-DFT deviations, we used a synthesizability threshold of $E^{\text{hull}} \leq 100$ meV/atom for the new charged/discharged compositions considered, i.e., compounds with $E^{\text{hull}} \leq 100$ meV/atom were considered (meta)stable.

For each (meta)stable compound, we subsequently computed the average intercalation voltage from the total energy difference between the discharged and charged compositions using the approximate Nernst equation, as shown in Equation (1) [100],

$$V = -\frac{\Delta G}{2Fx} \approx -\frac{E_{\text{discharged}} - E_{\text{charged}} - x \mu_{\text{Ca}}}{2Fx} \quad (1)$$

where $E_{\text{discharged}}$ and E_{charged} are the corrected MACE-calculated total energies of the discharged and charged structures, respectively. x is the number of intercalated Ca atoms per formula unit of a given charged composition, F is the Faraday constant, and μ_{Ca} is the chemical potential (energy per atom) of metallic calcium in its ground-state face-centered-cubic phase. The Gibbs energy change in Equation 1 is approximated by the total energy difference ($\Delta G \approx \Delta E$), neglecting pV and entropic contributions, consistent with typical high-throughput DFT workflows.

2.5 Structure curation for Ca-mobility estimation

In order to uniquely identify candidate structures for the computationally-intensive Ca-mobility estimations, we removed duplicacy among the screened frameworks by first grouping entries based on composition in the discharged state. Subsequently, we clustered the corresponding structures within each group based on crystallographic similarity using `pymatgen`’s `StructureMatcher` with its default tolerances (i.e., being symmetry- and scale-aware, species-sensitive). From each cluster of ‘similar’ structures, we retained the entry with the lowest E^{hull} , yielding a non-redundant set of compositionally unique structures with high thermodynamic (meta)stability.

As an additional redundancy check, we cross-examined the structural similarity of candidate structures obtained against available MP structures using `StructureMatcher` (default tolerances). We grouped our screened structures by composition in the discharged state and subsequently compared the discharged structures within each each group with available MP structures with the same composition. We eliminated identified candidates that matched with structures in the MP and were previously studied as possible Ca cathodes (e.g. $\text{CaV}_2(\text{PO}_4)_3$, [51, 54] CaV_2O_5 , [31] $\text{CaFe}_2(\text{SO}_4)_3$ [54]). On the other hand, MP-matched entries without prior Ca-cathode studies were retained for Ca-mobility evaluation. Note that we also removed compounds lacking viable Ca (de)insertion pathways for subsequent Ca-mobility calculations. Operationally, we defined structures lacking viable Ca (de)insertion pathways as those that exhibit (i) an absence of any pair of Ca-sites with hopping distances of $< 6 \text{ \AA}$, or (ii) the absence of a percolating network of Ca-sites enabling insertion/extraction as determined via visual inspection.

2.6 Migration barrier calculations

For selected frameworks with ‘small’ unit cells (i.e., lattice parameters $< 8 \text{ \AA}$), we constructed larger supercells of lattice parameters at least 8 \AA to avoid spurious interactions between the migrating Ca^{2+} and its periodic images. To assess Ca^{2+} mobility, we analyzed each discharged structure (unit or supercell) by explicitly visualizing and enumerating the relevant vacancy-mediated migration pathways, typically amounting from one to four per structure. Additionally, we recorded whether long-range transport of Ca required all of these pathways or only a subset to be active. To identify Ca-cathode candidates with acceptable rate performance, we consider a fairly liberal maximum allowed $E_m \approx 1 \text{ eV}$, which corresponds to a possibly reversible Ca (de)intercalation across cathode particles of $\sim 5 \text{ nm}$ characteristic size, and operating at 333 K (60 °C) and at C/10 rate. [35, 54, 55] Thus, we considered Ca^{2+} migration pathways exhibiting $E_m \leq 1 \text{ eV}$ to be electrochemically active.

For each pathway within a given structure, endpoint configurations (i.e., with the Ca^{2+} located at the start or the end sites) were generated and geometry-optimized using MACE with ASE’s `QuasiNewton` algorithm upto a force threshold of $|0.05| \text{ eV \AA}^{-1}$. Corresponding minimum-energy paths were computed using the NEB method in conjunction with MACE and the Broyden–Fletcher–Goldfarb–Shanno (BFGS [101]) algorithm

with a spring constant of 2.5 eV \AA^{-2} between images along the band. For each structure, we generated an initial band of nine images (seven intermediate images plus the endpoints) using the image-dependent pair potential [102] interpolation scheme, which was found to provide a better initial guess for migration pathways compared to linear interpolation in our previous benchmarks. [76] We considered the NEB calculations converged if the perpendicular component of the band force fell below $|0.05| \text{ eV \AA}^{-1}$ or the NEB optimization reached a maximum of 1,000 steps. The E_m was taken as the energy of the highest (saddle-point) image relative to the lowest energy image.

Alongside MACE, we used the Orb-v3 foundational model (conservative variant) as an independent comparator to cross-validate predictions and guide candidate down-selection for DFT-based NEB validation. The conservative Orb-v3 variant computes forces and stresses as analytic derivatives of the energy via backpropagation (which is desirable for NEB), and is designed for fast and accurate prediction across diverse inorganic materials. Notably, we considered MACE and Orb-v3 foundational models in this work based on prior benchmarking that demonstrated strong agreement of these models with DFT-computed E_m . [76] For Orb-v3 based calculations, we used the corresponding ASE calculator to evaluate E_m with the same NEB settings as for MACE, except that the endpoint structures were relaxed with the BFGS optimizer (rather than QuasiNewton) due to faster convergence based on our preliminary tests.

In addition to foundational MLIPs, we used a transfer-learning based property predictor graph model built on the ALIGNN architecture (hereafter referred to as TL) to predict E_m . [86, 88] ALIGNN encodes atomic, bond, and bond-angle information via edge-gated graph convolutions to produce a pooled crystal embedding that is mapped to E_m by a multilayer perceptron. [103] The TL model employed here was previously fine-tuned on a literature-derived dataset of 619 DFT-calculated E_m . [87] For each migration pathway considered, we provided a pathway-encoded input in which the migrating ion occupies the sites corresponding to the initial and final configurations together with three linearly interpolated intermediate images (i.e., an NEB-style initialization). With this band-like structural input, the TL model predicts the corresponding E_m for that pathway, which is used in conjunction with MACE and Orb-v3 predicted E_m values for DFT-NEB calculations.

2.7 DFT-NEB validation

For the candidates identified as exhibiting promising Ca mobility, based on MACE, Orb-v3, and TL model estimations, we validated the predictions using DFT-based NEB calculations. [89, 90] To generate the initial band for a DFT-NEB calculation, we first performed a short MACE-NEB run with five intermediate images to generate an initial Ca-migration pathway, leveraging the ability of MACE to provide an accurate geometric description of the band. [76] The corresponding endpoints (i.e., the initial and final images) were subsequently relaxed at the DFT level, and combined with the MACE-optimized intermediate images as the initial band for the DFT-NEB calculation. Thus, the (super)cell sizes used for DFT-NEB calculations were identical to prior (super)cells used for MACE, Orb-v3, and TL calculations.

All spin-polarized endpoint relaxations were performed with DFT using the Vienna *ab initio* simulation package [104, 105] and the Perdew–Burke–Ernzerhof functionalization of the generalized-gradient approximation [106] for electronic exchange and correlation, to minimize computational costs and mitigate convergence difficulties. [107] We employed projector augmented-wave [108, 109] potentials with frozen cores, used a plane-wave kinetic-energy cutoff of 520 eV, and sampled the irreducible Brillouin zone using Γ -centered Monkhorst–Pack [110] meshes with a minimum k -point grid density of 16 k -points per \AA . Endpoint relaxations were carried out at fixed cell shape and volume, without symmetry constraints, and with convergence

thresholds of 10^{-5} eV for the total energy and $|0.03|$ eV \AA^{-1} for the atomic forces. The DFT-powered NEB calculations used a spring constant of 5 eV \AA^{-2} between the adjacent images, with the NEB calculation considered converged when the maximum perpendicular force on the band fell below $|0.05|$ eV \AA^{-1} .

3 Results

3.1 Querying MP and target Ca-VPV window

Figure 2a represents the distribution of local environments containing Ca, as characterized by the Ca-VPV metric, among the 4,350 structures that comprise set 1 of MP-queried frameworks. Notably, we observe a tight clustering of Ca-containing local environments (blue shaded region) around the median Ca-VPV value of 13.86 \AA^3 (vertical dashed line in **Figure 2a**). The minimum and maximum value of Ca-VPV within our queried set are 9.85 and 49.00 \AA^3 , respectively. Additionally, our tolerance window of $\pm 5\%$ around the median gives us a target Ca-VPV window of 13.17 - 14.56 \AA^3 (purple band in **Figure 2a**) for determining geometric compatibility of possible sites to host Ca in novel frameworks (i.e., within set 2). Note that we use the $\pm 5\%$ tolerance window to capture natural variations in Ca coordination while keeping a tight geometric criterion to determine compatibility with a ‘typical’ coordination environment preferred by Ca.

To provide a quantitative overview of the availability of host frameworks that can accommodate Ca, we present the percentage distribution of queried candidate structures (totally 52,945) that form set 2 in **Figure 2b**. The structures are grouped by potential Ca-substitution sites, where X denotes vacancies/interstitials. As expected, Li-containing compounds dominate the distribution, accounting for 28.1%, reflecting the statistically large number of Li compounds present in MP. Li is followed by compounds with X sites (17.9%), Mg (13.0%), Na (7.3%), H (4.8%), Ba (4.3%), Sr (4.1%), and K (3.9%). There are several compounds containing cations such as Cu, Zn, W, etc., as possible substitutional sites for Ca, accounting for $\leq 3.5\%$ of the distribution. Compounds containing potential substitutional cations that account for $< 1\%$ of the queried data are grouped and represented as ‘Others’ (accounting for a total of 15.6% of the dataset). As a start of our screening approach (**Figure 1**), all structures contributing to the distribution in **Figure 2b** are passed through the Ca-VPV compatibility filter.

3.2 Geometric criterion screening

Upon applying the Ca-VPV tolerance window (**Figure 2a**) as a geometric compatibility check, our full dataset reduces from a total of 52,945 initial structures to 5,946 candidate compounds, highlighting the limited structural compatibility within the inorganic chemical space to host Ca. **Figure 2c** summarizes the statistical distribution of the VPV-matched set, shown alongside the entire queried dataset on a section of the periodic table. Cells corresponding to redox-active TMs and anions are shown as light red and light blue, respectively, and display only the element symbol (i.e., no numerical annotations), since these sites are not considered for potential replacement with Ca. Elements not present in the full dataset are either omitted or shown in gray for visual completeness. Ca, representing the substituting species, is indicated by the yellow-bordered cell shaded in dark green.

For each potential substitutional element (or X), the green heat map (upper triangles in **Figure 2c**) encodes the percentage of the filtered compounds that contain the element, i.e., the percentage of a given element-containing structures that satisfy the target Ca-VPV window. The corresponding percentage value is printed on the top of the cell alongside the element symbol in the upper triangle. The percentage of

the VPV-matched set, indicating a strong enrichment among the filtered compounds and a strong similarity in local environments inhabited by La with Ca. Other notable substitutional cations include Na (9.5% VPV-matched, 7.3% overall), Mg (6.1% VPV-matched, 13.0% overall), Nd (4.0% VPV-matched, 1.0% overall), and H (3.9% VPV-matched, 4.8% overall).

3.3 Filtering on charge neutrality

As a pre-requisite for thermodynamic (meta)stability, we evaluate the charge neutrality of the two end-member compositions of each VPV-matched candidate framework, namely, the fully discharged and the fully charged compositions. **Figure 3a** shows a heat map of the contingency matrix for charge neutrality in the charged and discharged compositions. Among 5,946 VPV-matched compounds, 31.3% (or 1,864) are not charge neutral in either state. Further, 27.4% (1,628) of frameworks are charge neutral only in the discharged state and 14.7% (873) are charge neutral only in the charged state. Finally, 26.8% (1,581) of the VPV-matched compounds are charge neutral in both charged and discharged compositions, thus representing the strongest set of candidates for further screening.

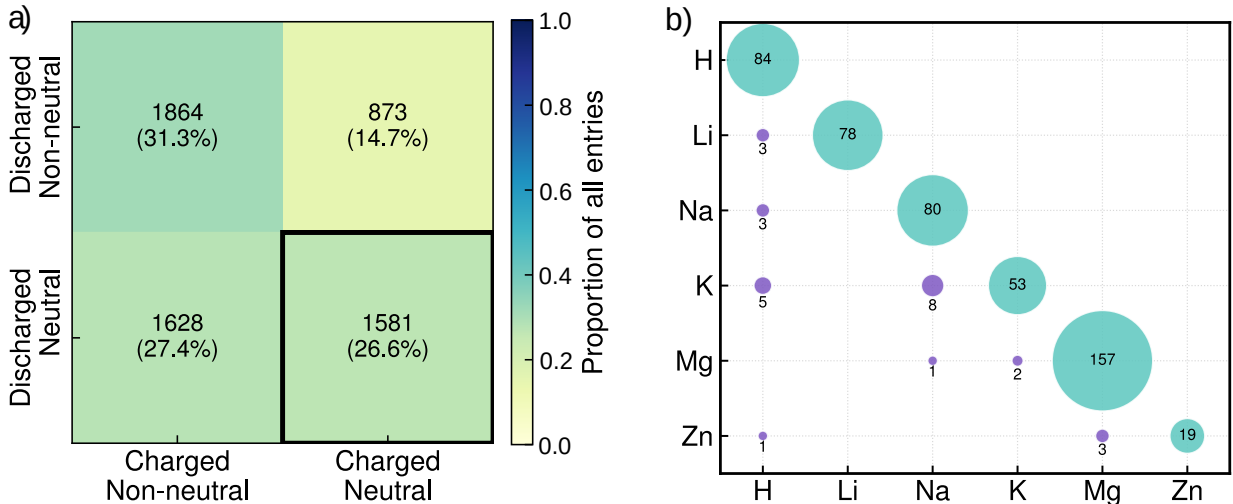


Figure 3: a) Contingency matrix of charge neutrality among discharged and charged compositions of VPV-matched compounds. b) Distribution of compounds removed due to the presence of non-Ca mobile cation(s).

3.4 Exclusion of mobile-cation-containing compounds

To ensure that Ca remains the electroactive ion, we exclude 445 compounds (out of 1,581 charge-neutral compounds) that host additional mobile cation(s), namely, H^+ , Li^+ , Na^+ , K^+ , Mg^{2+} , and Zn^{2+} . The statistics of the compounds removed due to the presence of a non-Ca mobile cation is presented as bubble plots in **Figure 3b**. The size of each bubble in **Figure 3b** is indicative of the number of excluded structures due to the presence of other mobile cation(s). Diagonal teal bubbles indicate the count of compounds that contain only the indicated mobile cation (besides Ca). For example, 157 structures are excluded due to the presence of only Mg as an additional mobile cation. Off-diagonal purple bubbles indicate the number of compounds in which the corresponding pair of mobile cations co-exist. For instance, 8 structures are excluded due to the presence of both Na^+ and K^+ in the structure. Finally, the application of this filter results in a total of 1,136 candidate compounds that only contain Ca as an electroactive ion.

3.5 Thermodynamic stability

We use E^{hull} to assess thermodynamic (meta)stability of the 1,129 screened cathode materials, [111] with **Figure 4a** showing the distribution of MACE-computed E^{hull} values. The reduction from 1,136 compounds (after excluding structures having non-Ca mobile cations) to 1,129 compounds is due to the lack of convergence in our MACE calculations for seven structures, all of which share the common feature that Ca substitutes H in the host structure. Specifically, **Figure 4a** displays the probability density from a kernel density estimate (KDE) with units of $1/\text{eV}$, as a function of E^{hull} , for both discharged (teal curve) and charged (purple curve) compositions. Both discharged and charged density curves are normalized independently such that the area under each curve equals 1, with their corresponding medians indicated as teal and purple vertical dotted lines, respectively. The density at a given E^{hull} in **Figure 4a** reflects the rate of occurrence of structures around the E^{hull} value, i.e., density at $E^{\text{hull}} \times \text{window of } E^{\text{hull}} = \text{fraction of compounds within that window around the } E^{\text{hull}}$. For example, a density of 5 at $E^{\text{hull}} = 0.05 \text{ eV/atom}$ on the discharged curve in **Figure 4a** indicates that 5% of the overall 1,129 discharged structures (~ 56 structures) occur within a 0.01 eV/atom window around $E^{\text{hull}} = 0.05 \text{ eV/atom}$ (i.e., $5 \times 0.01 = 0.05$ or 5%). The black vertical dashed line indicates the synthesizability heuristic, i.e., $E^{\text{hull}} = 100 \text{ meV/atom}$, [99] used in our study to identify frameworks that are possibly synthesizable. Thus, phases on the hull ($E^{\text{hull}} = 0$) are predicted ground states, whereas those with $0 < E^{\text{hull}} \leq 100 \text{ meV/atom}$ are considered metastable with respect to decomposition into other lower-energy phases. The E^{hull} range in **Figure 4a** is capped at the 99th percentile of values to avoid long tails dominating the plot.

Notably, the discharged and charged compositions exhibit distinct distributions, as highlighted by their corresponding median E^{hull} values of 85 and 69 meV/atom, respectively. Additionally, the value of E^{hull} with the highest density for discharged phases is 69 meV/atom, which is slightly higher compared to the corresponding peak for the charged phases (62 meV/atom). However, a similar fraction of charged compositions ($\sim 3\%$) and discharged compositions ($\sim 2\%$) are predicted to be stable, i.e., $E^{\text{hull}} = 0$. Although the marginally higher occurrence of (meta)stable charged compositions compared to discharged compositions reflects our workflow of targeting non-Ca-containing structures (**Figure 1**), we do expect experimental strategies targeting the synthesis of charged compositions (with subsequent electrochemical intercalation of Ca) to be statistically more successful compared to synthesizing discharged compositions with subsequent Ca removal. Finally, we observe a non-negligible subset of candidates exhibiting E^{hull} well beyond 100 meV/atom, indicating substantial thermodynamic driving forces for decomposition, making these phases unlikely to be accessible under conventional synthesis conditions.

While the majority of screened candidates cluster at low E^{hull} values at either their discharged or charged compositions, cathode candidates that exhibit $E^{\text{hull}} \leq 100 \text{ meV/atom}$ in both their discharged and charged states are promising as Ca-cathodes. To identify such candidates, we assign each screened framework to one of four categories, namely, (meta)stable in both discharged and charged states, (meta)stable only at discharged, (meta)stable only at charged, or unstable in both states, and visualize the statistics as a ‘Sankey’ diagram in **Figure 4b**. The left and right nodes of **Figure 4b** sum up to the (meta)stable and unstable discharged and charged compositions, respectively, with the thickness of the colored links indicating the number of compounds that overlap in the corresponding stability class.

Of the 1,129 frameworks evaluated, 653 discharged and 713 charged compositions are (meta)stable, as represented by light green nodes in **Figure 4b**, while 476 discharged and 416 charged compositions are unstable, as shown by light red nodes. Importantly, our stability screening identifies 481 frameworks that are (meta)stable in both their charged and discharged states, as highlighted by the green link, indicating

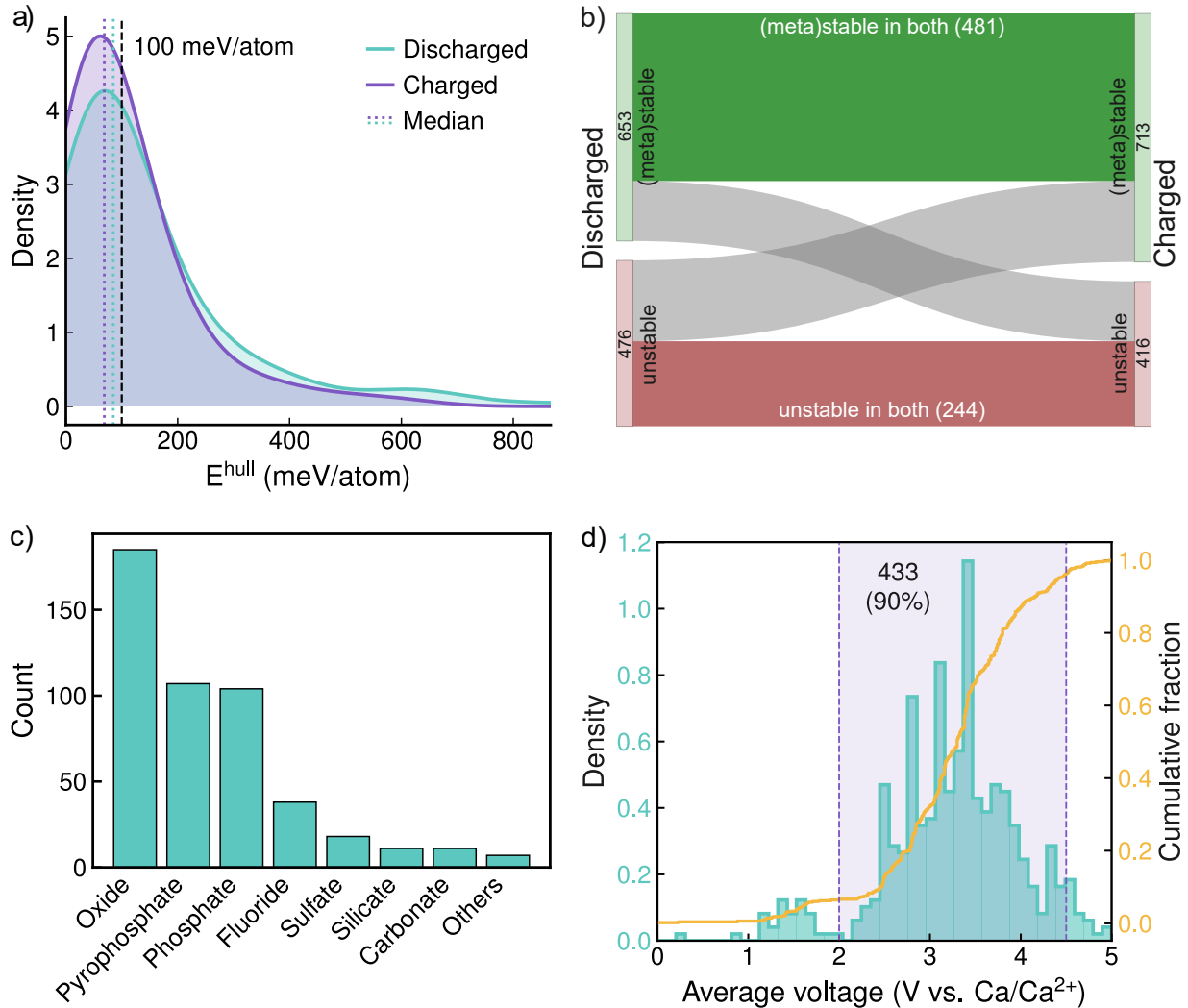


Figure 4: a) The E^{hull} distribution of the discharged (teal) and charged (purple) candidate compositions and their corresponding median values (vertical dotted lines). The black vertical dashed line marks the (meta)stability criterion ($E^{\text{hull}} = 100$ meV/atom). b) Sankey diagram tracing the thermodynamic (meta)stability of discharged and charged compositions. c) Screened (meta)stable frameworks grouped by chemistry. d) Computed average voltage (versus Ca metal) between the fully discharged and charged compositions for screened (meta)stable frameworks.

the most promising set of Ca-cathode candidates based on our threshold E^{hull} . Thus, we limit our voltage and Ca-mobility evaluations to these 481 frameworks that are (meta)stable in both their discharged and charged states. Also, we find 244 frameworks that are unstable in both discharged and charged states (red link), 172 frameworks that are (meta)stable in discharged but unstable in charged (thin grey link), and 232 frameworks that are (meta)stable in charged but unstable in discharged (thick grey link).

Figure 4c shows a histogram of the screened (meta)stable frameworks (i.e., 481 candidates) grouped by chemistry, namely, oxide, pyrophosphate, phosphate, fluoride, sulfate, silicate, carbonate, and others. Oxides dominate the set, followed, in decreasing abundance by pyrophosphates and phosphates. The dominance of oxides is in line with the overall data distribution in MP. Interestingly, we observe only a single chalcogenide (i.e., sulfide or selenide) host, namely $\text{CaTi}(\text{TlS})_4$, to be selected by our screening process thus far, possibly

indicating negligible occurrences of (meta)stable combinations of Ca, redox-active TM, and S/Se as the anion.

3.6 Average voltage

Figure 4d shows the distribution of average Ca intercalation voltages, versus Ca metal, calculated across the fully discharged and charged compositions, for the 481 frameworks that pass the thermodynamic (meta)stability filter. The teal bars (left y-axis) indicate the probability density of structures at a given average voltage (computed using a KDE with units of $1/V$, as obtained by normalizing the histogram such that the total area is 1) and the orange curve (right y-axis) signifies the cumulative fraction of structures over the spanned voltages. The density metric represents a rate of occurrence of structures within a voltage window, as a function of voltage, similar to the notation used in **Figure 4a**. We adopt a practical operating voltage window of 2.0–4.5 V (shaded region in **Figure 4d**), consistent with the electrochemical stability limits of current Ca electrolytes, [13, 30] and identify frameworks within this range as potential Ca-cathode candidates for subsequent mobility evaluation. Similar voltage windows have been used in past cathode screening studies as well. [35, 54, 55]

Notably, 433 out of 481 frameworks (90%) fall within the 2.0–4.5 V voltage interval, indicating substantial overlap between thermodynamic (meta)stability and electrochemical compatibility. The cumulative curve rises steeply across the 2.0–4.5 V region, reflecting this concentration of candidates in the practically relevant voltage range, with the curve flattening at both the low and high voltage ranges. The low-voltage tail below 2 V corresponds to frameworks that are more suitable as potential anodes, whereas the high-voltage tail above 4.5 V likely exceeds the oxidative stability limits of current electrolytes. Accordingly, the 433 frameworks within the 2.0–4.5 V window, which also satisfy the E^{hull} criterion, are advanced to the Ca-mobility screening (see below).

3.7 Structure curation for mobility analysis

Figure 5 summarizes the progressive de-duplication and curation of candidate frameworks for Ca^{2+} mobility analysis. The dark gray, teal, and light gray bars report, respectively, the number of frameworks prior to each curation step, those retained after the step, and those removed by that step, across three filters: structural de-duplication, overlap with MP entries, and the removal of frameworks corresponding to previously explored or non-viable Ca pathways. Starting from the 433 voltage-screened candidates, structural de-duplication eliminates 43 redundant entries, reducing the set to 390 unique frameworks. Subsequent removal of 19 structures that overlap with existing MP entries narrows the pool to 371 frameworks. A final filter that excludes frameworks previously explored as Ca cathodes and those lacking viable Ca (de)insertion pathways reduces the set to 221 candidates. Thus, the initial pool of 433 (meta)stable, voltage-compatible frameworks is distilled to 221 structurally unique, previously unexplored hosts with plausible Ca-migration pathways for subsequent Ca^{2+} mobility evaluation.

3.8 Ca mobility in candidate frameworks

Given the key role E_m plays in estimating ionic mobility in materials, we show the distribution of Ca^{2+} E_m values across the screened and curated candidates in **Figure 6a**. E_m predictions by MACE, Orb-v3 and the TL model are indicated by teal, orange, and purple violins, respectively. The inset bar plot in **Figure 6a** shows the number of compounds with one, two, three, or four distinct migration pathways.

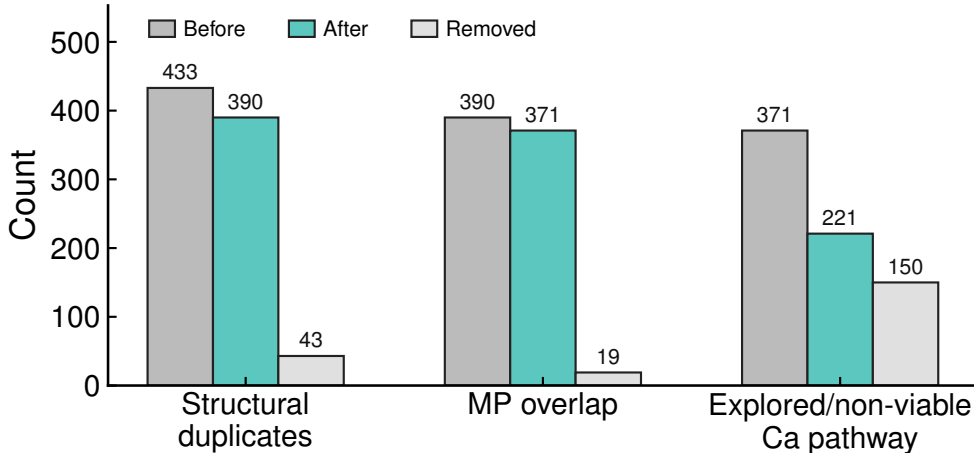


Figure 5: Sequence of data curation prior to Ca-mobility evaluation. Dark gray, teal, and light gray bars show the number of frameworks before each step, retained after the step, and removed by the step, respectively, for the three sequential filters considered.

In total, the dataset comprises 221 candidate frameworks spanning 299 unique migration pathways. For frameworks with multiple migration pathways, the active transport network may involve one, some, or all of these paths. However, we represent each framework by the median E_m across its distinct pathways for the purpose of considering statistical distribution of E_m . The embedded inner boxes within each violin spans the interquartile range (from the lower to the upper quartile), with the horizontal black line marking the median of the E_m distribution and black stars denoting outliers. The dashed horizontal gray line represents the E_m threshold of ~ 1 eV that we have used to identify Ca-cathode candidates with reasonable rate performance, a liberal threshold that is consistent with previous studies. [35, 54, 55] The number of candidates predicted to lie within this E_m threshold is indicated as text corresponding to each model.

With MACE predictions, the Ca^{2+} E_m span from 0.168 to 4.393 eV, with a median of 1.170 eV, indicating that the distribution is centered near 1 eV. Below the $E_m \leq 1$ eV threshold, MACE identifies 67 frameworks with reasonable Ca-mobility, representing the largest pool of promising Ca-cathode candidates among the three models considered. With respect to Orb-v3, its E_m predictions span a wider range than MACE (0.191–5.647 eV) with a higher median (1.281 eV), resulting in a E_m distribution that is broadly centered near ~ 1 eV but systematically shifted toward higher values with a pronounced tail beyond 3.5 eV. Under the $E_m \leq 1$ eV threshold, Orb-v3 selects 41 candidates, which is lower than the 67 identified by MACE. Finally, our TL model predicts a E_m range of 0.553–2.544 eV that is narrower than MACE and Orb-v3 but with a higher median of 1.535 eV, yielding only 10 candidates below the 1 eV threshold. The distribution of E_m values exhibited by the TL model is also qualitatively different from MACE and Orb-v3, as highlighted by the difference in the shape of the purple violin compared to the teal and orange violins in **Figure 6a**. Overall, the three models differ markedly in selectivity: MACE is the most permissive, retaining the largest number of frameworks under the 1 eV threshold, whereas the TL model is the most conservative.

Figure 6b compares the Ca^{2+} E_m predicted by Orb-v3 (orange circles) and the TL model (purple) against those obtained from MACE. A significant number of points cluster near the parity line (dashed grey), indicating that all three models capture moderately similar trends in E_m across the candidate set. Notably, Orb-v3 exhibits an almost linear correlation with MACE over the full E_m range, with a marginal tendency to predict higher values, consistent with our observations in **Figure 6a**. In contrast, the TL model

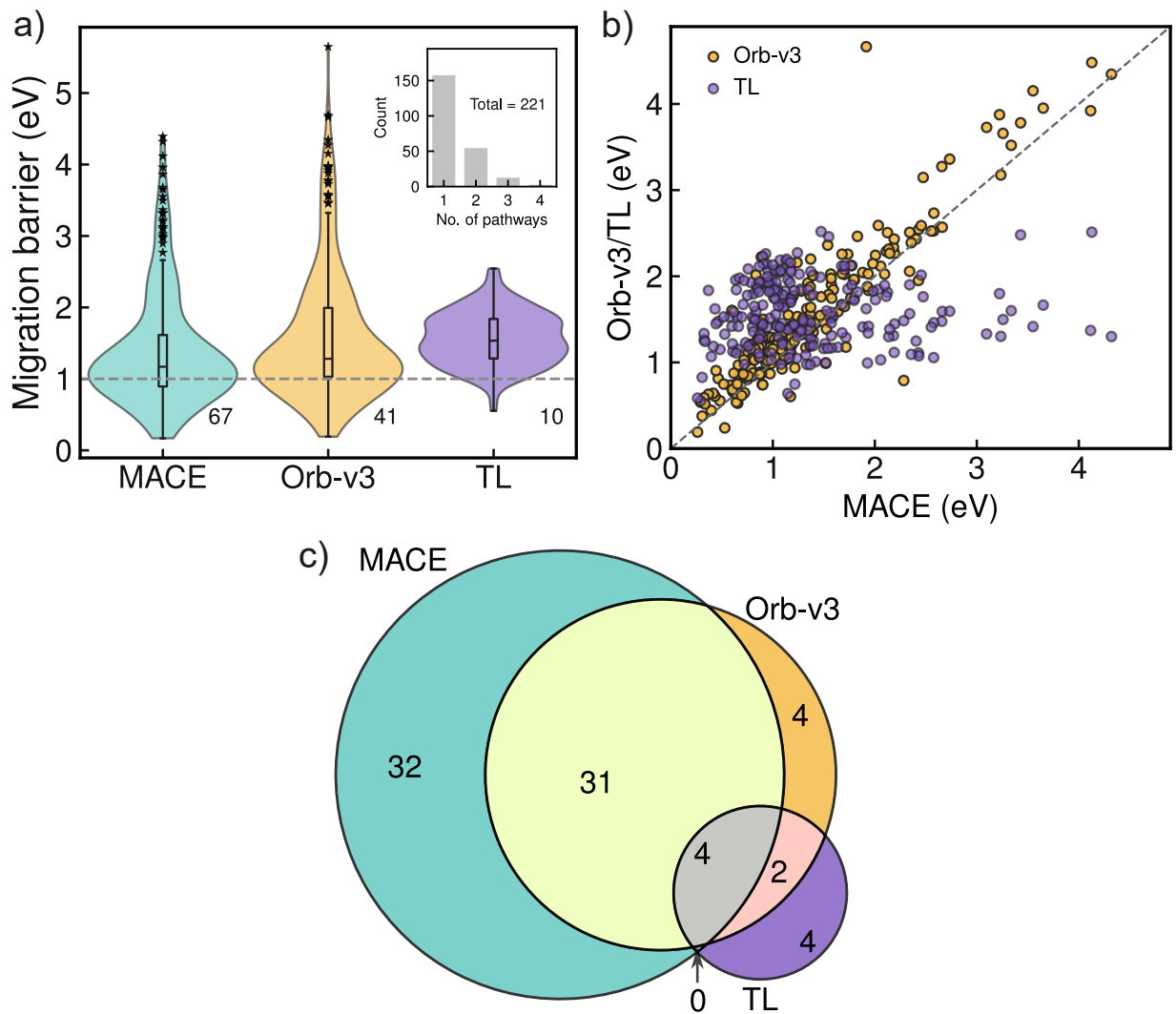


Figure 6: Ca^{2+} E_m within screened frameworks, as predicted by MACE (teal), Orb-v3 (orange), and TL (purple). a) Violin plot showing the distribution of E_m ; the inset bar chart reports the number of structures with one, two, three, and four distinct pathways. b) Parity plot comparing Orb-v3 and TL E_m values against MACE. c) Venn diagram of the overlap in selected candidate frameworks among the three models.

offers a more conservative E_m landscape, assigning higher values at low-to-intermediate MACE- E_m and lower values at high MACE- E_m . Thus, the TL model does exhibit qualitative differences compared to both MACE and Orb-v3, and identifies fewer candidates with Ca-mobility, which is consistent with its higher precision in identifying ‘good’ conductors. [88] Nevertheless, the TL model adds complementary information to MACE/Orb-v3 predictions and supports a more robust estimation of Ca^{2+} mobility across the candidate space.

To avoid over-reliance on any single model among MACE, Orb-v3, and TL for E_m predictions, we use an ensemble (or MoE) approach in which frameworks predicted favorably by at least two of the three models are considered as candidate Ca-cathodes, with a subset of them validated with DFT-NEB subsequently. **Figure 6c** illustrates the overlap among the model-selected candidates. Applying the E_m threshold yields 67, 41, and 10 candidates for MACE, Orb-v3, and TL, respectively. Since each model selects distinct, non-

overlapping frameworks and the pairwise overlaps among the models differ, no single model is an obvious arbiter. Notably, all three models share four common candidates (gray region). The overlap between MACE and Orb-v3 comprises 35 candidates in total (31 shared only by MACE and Orb-v3 and the four shared by all models; light yellow and gray regions). MACE and TL share four candidates, all of which are in the three-way overlap. Orb-v3 and TL share six candidates, i.e., two shared only by these two models plus the four shared by all three. Therefore, applying the ensemble approach, we arrive at a final set of 37 candidate Ca-cathode frameworks (green, gray, and pink regions in **Figure 6c**) that should exhibit reasonable Ca-mobility.

3.9 DFT-NEB validation

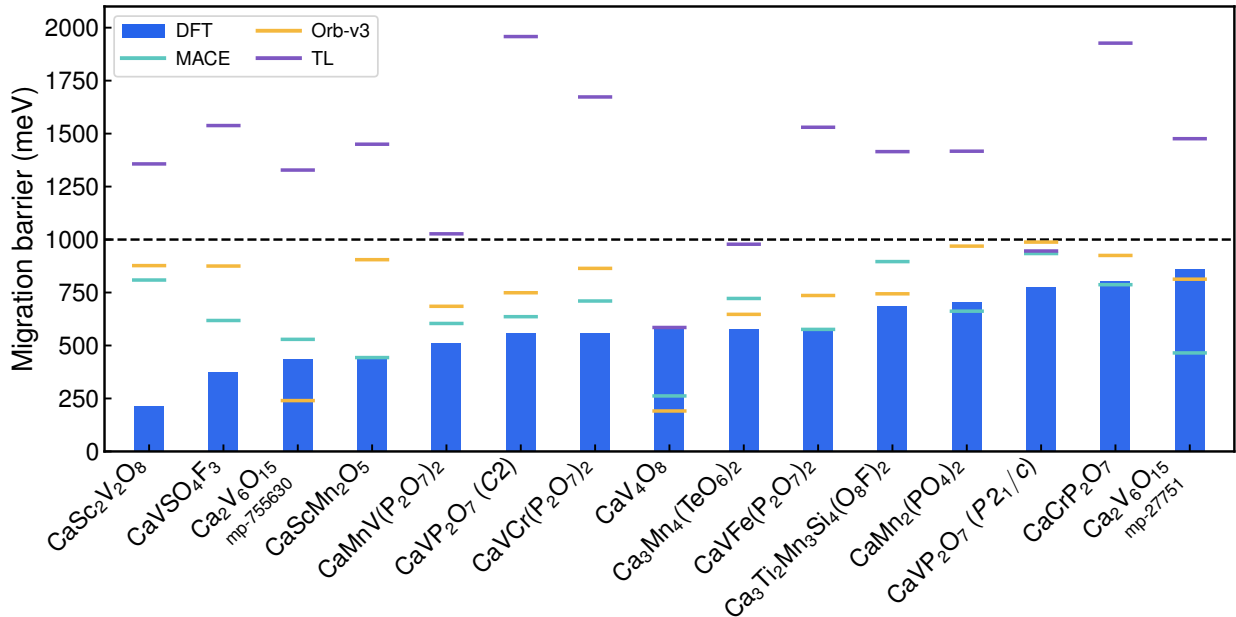


Figure 7: DFT-NEB E_m for a subset of final candidate frameworks, shown alongside predictions from MACE (teal), Orb-v3 (orange), and TL (purple) overlaid as horizontal lines on each bar. The dashed black line marks the 1000 meV threshold. Space groups of select structures are indicated in parentheses. Compounds with the same chemical formula and space group but different StructureMatcher assignments are distinguished by their MP IDs.

To reduce computational cost associated with DFT-NEB calculations and validate as many of the ensemble-model-predicted Ca-cathode candidates, we excluded structures sharing the same composition and space group that are classified as distinct by `pymatgen`'s `StructureMatcher` due to minor atomic rearrangements, except $\text{Ca}_2\text{V}_6\text{O}_{15}$. This reduction yields 26 distinct frameworks for DFT-NEB calculations. **Figure 7** presents a bar plot of DFT-estimated E_m alongside the corresponding MACE, Orb-v3, and TL predictions for a subset containing 15 frameworks (14 distinct frameworks + 1 additional $\text{Ca}_2\text{V}_6\text{O}_{15}$) for which DFT-NEB calculations converged, namely, $\text{CaSc}_2\text{V}_2\text{O}_8$, CaVSO_4F_3 , $\text{Ca}_2\text{V}_6\text{O}_{12}$ (MP ID: mp-755630), $\text{CaScMn}_2\text{O}_5$, $\text{CaMnV}(\text{P}_2\text{O}_7)_2$, CaVP_2O_7 ($C2$), $\text{CaVCr}(\text{P}_2\text{O}_7)_2$, CaV_4O_8 , $\text{Ca}_3\text{Mn}_4(\text{TeO}_6)_2$, $\text{CaVFe}(\text{P}_2\text{O}_7)_2$, $\text{Ca}_3\text{Ti}_2\text{Mn}_3\text{Si}_4(\text{O}_8\text{F})_2$, $\text{CaMn}_2(\text{PO}_4)_2$, CaVP_2O_7 ($P2_1/c$), CaCrP_2O_7 , and $\text{Ca}_2\text{V}_6\text{O}_{15}$ (MP ID: mp-27751). Polymorphs with the same composition are distinguished by listing their space group from the original MP structure in parentheses. In the case of $\text{Ca}_2\text{V}_6\text{O}_{15}$, we include two structures classified as distinct by `StructureMatcher` despite identical composition and space group, for additional validation. The DFT-NEB-

calculated minimum energy pathways of Ca^{2+} migration for the 15 frameworks are compiled in **Figure S2**. Note that our DFT-NEB calculations did not successfully converge for the remaining 12 frameworks.

Importantly, the DFT-computed E_m , for all frameworks whose calculations converged, lie within the tolerance threshold of $E_m < 1000$ meV (black dashed line in **Figure 7**) adopted in this study, validating the ability of our model ensemble to reliably identify promising Ca cathode candidate frameworks. To gain further confidence in our ensemble predictions, we expanded the validation by randomly sampling a subset of three non-shortlisted candidates, and found good agreement with DFT-NEB calculations for such structures as well (see **Figures S3** and **S4**). Among the ML models, MACE (teal lines in **Figure 7**) shows the best agreement with DFT, yielding a mean absolute error (MAE) against all DFT-calculated (including the non-candidates) E_m of 161 meV and closely reproducing the overall trend of the barriers across the dataset. Orb-v3 (orange lines) exhibits larger deviations with an MAE of 274 meV, generally capturing the qualitative trends but often overestimating E_m . Interestingly, the TL model (purple lines) shows substantially larger discrepancies, with an MAE of 671 meV, and a tendency to significantly overestimate E_m . Taken together, these results suggest that MACE reproduces the DFT E_m more closely compared to the other models considered.

Notably, we identify $\text{CaSc}_2\text{V}_2\text{O}_8$ and CaVSO_4F_3 to exhibit the lowest DFT-calculated E_m of 213 and 376 meV, respectively, with both values being two of the lowest Ca^{2+} E_m reported in the literature so far. Other candidate structures exhibiting DFT-NEB $E_m < 500$ meV, which is an indicator of facile Ca^{2+} motion under typical electrochemical conditions, are $\text{CaScMn}_2\text{O}_5$ (447 meV), and $\text{Ca}_2\text{V}_6\text{O}_{15}$ (MP ID: mp-755630; 438 meV). Given the systematic (and qualitative) agreement between the ensemble-classification of structures with reasonable Ca-mobility and low E_m with DFT, we consider the full set of 37 frameworks identified by our MoE predictions to be promising Ca-cathode candidates. The 37 frameworks do contain multiple polymorphs of the same composition, thus resulting in a total of 25 distinct and promising Ca-cathode compositions. We summarize the Ca^{2+} E_m calculated using MACE, Orb-v3, TL, and/or DFT for the 37 identified Ca cathode frameworks, along with their compositions, space groups, MP-IDs, and other screening metrics computed in this work in **Table 1**. Schematics of all 37 structures are compiled in **Figures S5-S8** of the SI. Among the 25 promising compositions, we highlight $\text{Ca}_3(\text{CoO}_2)_4$, $\text{Ca}_3\text{Mn}_4(\text{TeO}_6)_2$, CaVF_5 , and CaVSO_4F_3 due to their thermodynamic stability in the charged state ($E^{\text{hull}} = 0$ meV/atom), signifying their thermodynamic accessibility and potentially successful experimental synthesis.

4 Discussion

In this work, we have performed a large-scale screening of potential Ca battery cathodes across 52,945 non-Ca-containing MP structures using a high-throughput workflow (**Figure 1**) accelerated by foundational ML models. We have applied a series of chemically and physically motivated filters, namely, geometry-based VPV (**Figure 2**), electrostatic charge neutrality and presence of non-Ca mobile cations (**Figure 3**), thermodynamic (meta)stability and average intercalation voltage (**Figure 4**), duplicate structures (**Figure 5**), and Ca^{2+} mobility (**Figure 6**), to down-select a final list of 37 distinct structures spread across 25 distinct compositions. Importantly, a section of our Ca-mobility estimates have been validated with computationally-heavy DFT-NEB calculations (**Figure 7**), which are in good agreement with our ensemble approach of selecting candidates with reasonable E_m . We illustrate the overall screening workflow in **Figure 8**, with **Table 1** and **Figures S5-S8** compiling all the candidates identified.

In our screening strategy, the Ca-VPV descriptor was constrained by a relatively strict tolerance window

Table 1: Summary of Ca-cathode candidates identified in this work. For each framework, we report the composition, space group, MP-ID, substituted site and the VPV, E^{hull} at discharged and charged compositions, average voltage versus Ca metal, and Ca^{2+} E_m obtained from DFT, MACE, Orb-v3, and TL. Two E_m for a given framework indicate two distinct migration pathways. Missing DFT values correspond to polymorphs excluded or non-convergence of NEB calculations.

Composition	Space group	MP-ID	Substituted site (VPV; \AA^3)	E^{hull} (meV/atom)		Average voltage (V vs. Ca)	Ca^{2+} E_m (meV)		
				Discharged	Charged		DFT	MACE	Orb-v3
$\text{Ca}_3(\text{CoO}_2)_4$	<i>Pmmn</i>	mp-766225	Na (13.29)	99	0	4.5	307	377	827
$\text{Ca}_3\text{Mn}_4(\text{TeO}_6)_2$	<i>Pnma</i>	mp-561325	Na (14.07)	71	0	4.1	594	722	647 978
$\text{CaCo}_3\text{NiO}_8$	<i>R3m</i>	mp-2219095	Mg (13.88)	68	43	3.4	292	538	553
		mp-764481	Li (13.26)	38			640	638	1110
		mp-764622	Li (13.33)	36			759	841	1190
		mp-764488	Li (13.34)	36			511	604	685 1215
		mp-764484	Li (13.36)	39	16	3.8	982	985	1027
$\text{CaMnV}(\text{P}_2\text{O}_7)_2$	<i>P1</i>	mp-759232	Li (13.51)	36			733	833	1228
		mp-764480	Li (13.36)	38			872	862	1061
		mp-758360	Li (14.28)	12	10	2.9	776	934	988 1933
		mp-2217313	Mg (13.47)	6	36	3.1	558	636	749 1958
		mp-752490	Li (13.55)	21	24	3.8	583	576	736 1530
$\text{CaVFe}(\text{P}_2\text{O}_7)_2$	<i>P1</i>	mp-1235847	Li (14.53)	24	24	3.7	801	842	1526
		mp-765981	Li (13.32)	24	24	3.7	652	750	1535
		mp-1235226	Li (13.20)	30	25	3.7	433	608	1622
CaCoP_2O_7	<i>P1</i>	mp-1569230	Li (14.11)	46	59	4.4	973	869	1514
CaCrP_2O_7	<i>P2_1</i>	mp-19103	Li (13.31)	34	41	3.4	802	787	925 1927
CaVPO_5	<i>Pnma</i>	mp-760911	Na (13.40)	84	29	3.1	416	641	1186
CaVF_5	<i>P2_1/c</i>	mp-759186	Li (13.24)	81	0	4.0	827	753	1777
		mp-759086	Li (13.38)	88	24	4.2	948	987	2080
CaVSO_4F_3	<i>P1</i>	mp-769603	Li (14.02)	11	0	4.1	376	618	875 1586
$\text{CaVCr}(\text{P}_2\text{O}_7)_2$	<i>P1</i>	mp-766000	Li (13.41)	37	41	3.6	560	710	864 1673
$\text{CaV}_3\text{Fe}_2\text{CuO}_{12}$	<i>P1</i>	mp-766078	Li (14.50)	42	60	3.6	901	740	1441
$\text{Ca}_3\text{Ti}_2\text{Mn}_3\text{Si}_4(\text{O}_8\text{F})_2$	<i>P2_1/c</i>	mp-1210891	Na (13.86)	33	81	2.9	686	896	744 1415
$\text{Ca}_2\text{V}_4\text{OF}_{12}$	<i>P1</i>	mp-757416	Li (13.55)	60	59	3.1	674	856	1978
$\text{CaScMn}_2\text{O}_5$	<i>Cmcm</i>	mp-770412	X (13.59)	90	58	2.5	447	443	905 1450
$\text{Ca}_2\text{V}_9\text{O}_{22}$	<i>P2_1/m</i>	mp-849581	X (13.50)	68	52	3.4	335	517	1244
		mp-769550	Li (13.47)	71	99	3.2	321	335	1059
$\text{Ca}_2\text{Mn}_5(\text{FeO}_6)_2$	<i>Cc</i>	mp-769550	Li (13.47)	71	99	3.2	472	550	1077
CaMnO_2	<i>P6_3/mmc</i>	mp-971647	Na (13.75)	84	78	2.5	1216	936	747
CaMnCSO_7	<i>P2_1</i>	mp-754499	Li (13.43)	44	7	4.0	1519	990	997
		mp-27751	Li (13.38)	65	57	3.4	859	529	240 1328
$\text{Ca}_2\text{V}_6\text{O}_{15}$	<i>C2/m</i>	mp-755630	Li (14.48)	55	56	3.4	438	465	813 1476
		mp-1234013	Mg (13.61)	42	41	3.2	482	554	1150
$\text{CaMn}_2(\text{PO}_4)_2$	<i>P1</i>	mp-1176722	Li (13.80)	48	34	3.5	704	662	969 1417
$\text{Ca}_5\text{V}_{18}\text{O}_{44}$	<i>Pm</i>	mp-773027	Li (13.98)	54	52	3.4	325	589	1334
$\text{CaSc}_2\text{V}_2\text{O}_8$	<i>C2</i>	mp-2218897	Mg (13.22)	76	34	2.6	213	809	877 1357
CaV_4O_8	<i>C2/m</i>	mp-2220145	Mg (13.89)	89	64	2.5	576	262	191 585

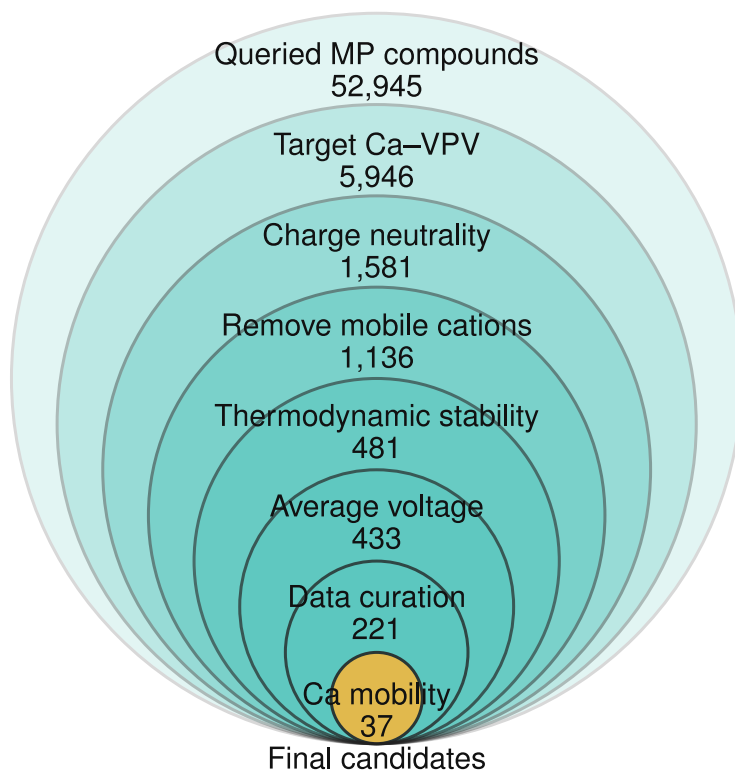


Figure 8: Summary of the Ca-cathode screening process. The concentric circles show the sequential filtering of structures and the number of compounds remaining after each screening step.

of $\pm 5\%$ around the Ca-VPV median (**Figure 2**). This strict choice prioritizes frameworks whose local environments are most similar to those in Ca-containing frameworks, while keeping the number of candidates manageable after applying all subsequent filters. In principle, the tolerance window can be broadened to include additional candidates. However, as one moves progressively farther from the Ca-VPV median, the likelihood of identifying candidate frameworks that are thermodynamically (meta)stable is expected to decrease, possibly reducing overall screening efficiency. Based on the final set of candidates listed in **Table 1**, the substituted cations/sites are predominantly Li, Na, Mg, and X, in descending order, suggesting that these species frequently provide structurally compatible host environments for Ca substitution and may therefore serve as practical starting points for Ca-cathode framework design. We note, however, that the prominence of Li-, Na-, and Mg-containing frameworks partly reflects their higher representation within the MP database, which increases their likelihood of appearing in the screened candidate set.

We evaluated charge neutrality (**Figure 3**) and thermodynamic stability (**Figure 4**) only for the fully charged and fully discharged compositions for any candidate framework, as explicitly sampling intermediate compositions would require exhaustive enumeration of Ca-vacancy configurations, which is computationally prohibitive in a high-throughput setting. Although such intermediate-state sampling could reveal additional charge-neutral and (meta)stable phases and thereby expand the pool of promising candidates, we do not capture any partially (de)intercalated compositions here, highlighting the need for more efficient methods to approximate intermediate-composition energetics in any follow-up large-scale screenings of Ca cathodes and beyond. Note that our average voltage calculations are also reported across the entire Ca-composition range (i.e., fully charged to fully discharged), where local variations in the voltage with Ca (de)intercalation can

result in possible bottlenecks in the practical use of any candidate with electrolytes. One possible strategy to account for partial Ca compositions is to focus on only thermodynamically stable (i.e., $E^{\text{hull}} = 0$ meV/atom) charged or discharged compositions (so that the likelihood of experimental synthesis is high) and perform a sub-sampling of intermediate Ca compositions by partial (de)intercalation, to reduce the compositional complexity.

One of the key bottlenecks in our screening workflow is the structural analysis required for assessing Ca^{2+} mobility, which presently involves visually inspecting each structure to identify all plausible migration pathways (**Figure 5**). This step quickly becomes intractable in a truly high-throughput setting, where hundreds to thousands of candidate frameworks may need to be analyzed, and therefore limits the overall speed and scalability of the workflow. Developing robust, automated tools to systematically generate and rank migration pathways would thus be highly valuable for the community, enabling more efficient screening of potential ionic conductors and facilitating the extension of similar workflows to even larger chemical and structural design spaces.

Since a rigorous validation of the E^{hull} for any screened Ca-cathode would require computing ground-state energies for all competing phases in the relevant chemical space (elemental, binary, ternary, quaternary, etc.), which can be computationally prohibitive in a high-throughput setting, we did not explicitly validate the thermodynamic stability of the identified candidates with DFT. However, most of the screened frameworks lie only marginally above the convex hull (typically ≤ 50 meV/atom, as shown in **Table 1**), and state-of-the-art ML models have been extensively benchmarked for accurate prediction of formation energies in inorganic systems. [112–114] Therefore, we expect that the majority of the screened candidates will remain thermodynamically accessible and, in principle, synthesizable. For the final set of candidates identified by the ensemble of models (**Figure 6**), we further validated the transport properties for a subset of 15 candidates by explicitly computing Ca E_m using DFT-based NEB calculations (**Figure 7**), thus increasing the confidence of our predictions. Given our limited dataset of 15 DFT-NEB calculated E_m values, we observe MACE to provide the closest agreement to DFT-values compared to Orb-v3 and TL.

While geometric descriptors such as the VPV provide an efficient and scalable way to identify geometrically-compatible Ca insertion sites, other approaches may also offer complementary insights for Ca-cathode discovery. In particular, insertion-site prediction based on the electronic charge density of the empty host framework has been proposed recently for Li-ion cathodes, where favorable cationic positions are identified by locating regions of low electronic charge density within the host lattice. [115] Since cations tend to occupy electrostatic potential minima, this approach provides a chemically informed route to identify stable insertion sites without prior knowledge of the fully intercalated structure. Such charge-density-guided insertion strategies may be particularly relevant for multivalent ions, such as Ca^{2+} , whose stronger electrostatic interactions with the host lattice play an important role in determining site stability. Exploring these electronic-structure-based descriptors alongside geometric approaches, such as VPV, could therefore provide additional opportunities for guiding the future design of battery electrode materials.

5 Conclusion

Accelerating the design and discovery of cathode frameworks capable of reversibly intercalating Ca^{2+} is essential for advancing multivalent CBs as practical alternatives to LIBs. Here, we used a combination of geometric, electrostatic, thermodynamic, and kinetic descriptors to screen across 52,945 non-Ca-containing structures within the MP database and identify 37 promising and distinct structures spanning across 25

different cathode compositions. Specifically, we introduced a geometry-based screening metric that evaluates the compatibility of potential Ca^{2+} sites within a structure using local VPV derived from Voronoi tessellation, providing a purely geometric and therefore transferable metric that avoids the limitations of ionic-radius-based heuristics across diverse bonding environments. Building on the geometric-screening and excluding structures that are non-charge-neutral and contain non-Ca mobile cations, we develop a scalable high-throughput framework in which foundational MLIPs (MACE in this work) accelerates the evaluation of ground-state energetics for thermodynamic stability and average voltage calculations, thereby resulting in a swift filtering of 433 candidates. For the evaluation of Ca^{2+} E_m , we used a combination of ML models, including MACE, Orb-v3, and TL, in a consensus ensemble approach to increase the confidence and robustness of E_m predictions. Notably, we selected promising candidates as those identified by at least 2 models to have E_m lower than our threshold of 1 eV, resulting in the filtering of 37 promising Ca-cathode frameworks. Finally, we corroborate our ensemble-selected Ca-cathodes with DFT-NEB calculations on a representative subset, thus validating the robustness of our selection and accuracy of E_m predictions. Importantly, our screening identifies two cathode candidates with swift Ca^{2+} mobility ($\text{CaSc}_2\text{V}_2\text{O}_8$, and CaVSO_4F_3) and four candidates with thermodynamic stability in their charged state ($\text{Ca}_3(\text{CoO}_2)_4$, $\text{Ca}_3\text{Mn}_4(\text{TeO}_6)_2$, CaVF_5 , and CaVSO_4F_3). Overall, our study demonstrates an effective strategy for accelerating Ca-cathode discovery and highlights the value of integrating transferable geometric descriptors, foundational ML models, and ensemble decision-making for materials exploration across broad chemical and structural spaces, paving the way for accelerated discovery in other intercalation chemistries and applications beyond batteries.

Acknowledgments

G.S.G. acknowledges the financial support received from the Science and Engineering Research Board (SERB), Department of Science and Technology, Government of India, under sanction number IPA/2021/000007. D.B.T. and A.K.B. acknowledge financial assistance from the Indian Institute of Science (IISc) and the Ministry of Education, Government of India, respectively. The authors acknowledge the computational resources provided by the Supercomputer Education and Research Centre (SERC) at IISc, which were instrumental in carrying out the first-principles calculations and high-throughput screening workflows presented in this thesis. The authors also gratefully acknowledge the Jülich Supercomputing Centre at Forschungszentrum Jülich, Germany, for access to the JURECA supercomputer under projects hpc-prf-emdft and hpc-prf-desal, which enabled some of the NEB calculations reported in this work.

Data and code availability

All calculated data and the scripts used in this work are available freely online on our GitHub repository.

Conflicts of interest

The authors have no conflicts of interest to declare.

References

- [1] M Stanley Whittingham. Ultimate limits to intercalation reactions for lithium batteries. *Chemical Reviews*, 114(23):11414–11443, 2014.
- [2] Arumugam Manthiram. A reflection on lithium-ion battery cathode chemistry. *Nature communications*, 11(1):1550, 2020.
- [3] Dominique Larcher and Jean-Marie Tarascon. Towards greener and more sustainable batteries for electrical energy storage. *Nature Chemistry*, 7(1):19–29, 2015.
- [4] Zachary P Cano, Dustin Banham, Siyu Ye, Andreas Hintennach, Jun Lu, Michael Fowler, and Zhongwei Chen. Batteries and fuel cells for emerging electric vehicle markets. *Nature Energy*, 3(4):279–289, 2018.
- [5] Jean-Marie Tarascon. Material science as a cornerstone driving battery research. *Nature Materials*, 21(9):979–982, 2022.
- [6] Björn Nykvist and Måns Nilsson. Rapidly falling costs of battery packs for electric vehicles. *Nature Climate Change*, 5(4):329–332, 2015.
- [7] Gavin Harper, Roberto Sommerville, Emma Kendrick, Laura Driscoll, Peter Slater, Rustam Stolkin, Allan Walton, Paul Christensen, Oliver Heidrich, Simon Lambert, et al. Recycling lithium-ion batteries from electric vehicles. *nature*, 575(7781):75–86, 2019.
- [8] Alvaro Masias, James Marcicki, and William A Paxton. Opportunities and challenges of lithium ion batteries in automotive applications. *ACS energy letters*, 6(2):621–630, 2021.
- [9] Alexandre Ponrouch, Jan Bitenc, Robert Dominko, Niklas Lindahl, Patrik Johansson, and M Rosa Palacín. Multivalent rechargeable batteries. *Energy Storage Materials*, 20:253–262, 2019.
- [10] Pieremanuele Canepa, Gopalakrishnan Sai Gautam, Daniel C Hannah, Rahul Malik, Miao Liu, Kevin G Gallagher, Kristin A Persson, and Gerbrand Ceder. Odyssey of multivalent cathode materials: open questions and future challenges. *Chemical Reviews*, 117(5):4287–4341, 2017.
- [11] Lauren E Blanc, Dipan Kundu, and Linda F Nazar. Scientific challenges for the implementation of zn-ion batteries. *Joule*, 4(4):771–799, 2020.
- [12] John Muldoon, Claudiu B Bucur, and Thomas Gregory. Quest for nonaqueous multivalent secondary batteries: magnesium and beyond. *Chemical Reviews*, 114(23):11683–11720, 2014.
- [13] Alexandre Ponrouch, Carlos Frontera, Fanny Bardé, and M Rosa Palacín. Towards a calcium-based rechargeable battery. *Nature Materials*, 15(2):169–172, 2016.
- [14] M Elena Arroyo-de Dompablo, Alexandre Ponrouch, Patrik Johansson, and M Rosa Palacín. Achievements, challenges, and prospects of calcium batteries. *Chemical Reviews*, 120(14):6331–6357, 2019.
- [15] Meng Wang, Chunlei Jiang, Songquan Zhang, Xiaohe Song, Yongbing Tang, and Hui-Ming Cheng. Reversible calcium alloying enables a practical room-temperature rechargeable calcium-ion battery with a high discharge voltage. *Nature chemistry*, 10(6):667–672, 2018.

- [16] Bifa Ji, Haiyan He, Wenjiao Yao, and Yongbing Tang. Recent advances and perspectives on calcium-ion storage: key materials and devices. *Advanced Materials*, 33(2):2005501, 2021.
- [17] Zhirong Zhao-Karger, Yanlei Xiu, Zhenyou Li, Adam Reupert, Thomas Smok, and Maximilian Fichtner. Calcium-tin alloys as anodes for rechargeable non-aqueous calcium-ion batteries at room temperature. *Nature communications*, 13(1):3849, 2022.
- [18] M Elena Arroyo-de Dompablo, Christopher Krich, Jessica Nava-Avenidaño, Neven Biskup, M Rosa Palacin, and Fanny Bardé. A joint computational and experimental evaluation of camn2o4 polymorphs as cathode materials for ca ion batteries. *Chemistry of Materials*, 28(19):6886–6893, 2016.
- [19] Deyana S Tchitchekova, Alexandre Ponrouch, Roberta Verrelli, Thibault Broux, Carlos Frontera, Andrea Sorrentino, Fanny Bardé, Neven Biskup, M Elena Arroyo-de Dompablo, and M Rosa Palacin. Electrochemical intercalation of calcium and magnesium in tis2: fundamental studies related to multivalent battery applications. *Chemistry of Materials*, 30(3):847–856, 2018.
- [20] M Elena Arroyo-de Dompablo, Christopher Krich, Jessica Nava-Avenidaño, M Rosa Palacín, and Fanny Bardé. In quest of cathode materials for ca ion batteries: the camo 3 perovskites (m= mo, cr, mn, fe, co, and ni). *Physical Chemistry Chemical Physics*, 18(29):19966–19972, 2016.
- [21] Arturo Torres, F Bardé, and María Elena Arroyo-de Dompablo. Evaluation of cobalt oxides for calcium battery cathode applications. *Solid State Ionics*, 340:115004, 2019.
- [22] Abhinandan Shyamsunder, Lauren E Blanc, Abdeljalil Assoud, and Linda F Nazar. Reversible calcium plating and stripping at room temperature using a borate salt. *ACS Energy Letters*, 4(9):2271–2276, 2019.
- [23] Da Wang, Xiangwen Gao, Yuhui Chen, Liyu Jin, Christian Kuss, and Peter G Bruce. Plating and stripping calcium in an organic electrolyte. *Nature materials*, 17(1):16–20, 2018.
- [24] Juan Forero-Saboya, Carine Davoisne, Rémi Dedryvère, Ibraheem Yousef, Pieremanuele Canepa, and Alexandre Ponrouch. Understanding the nature of the passivation layer enabling reversible calcium plating. *Energy & Environmental Science*, 13(10):3423–3431, 2020.
- [25] Ziqin Rong, Rahul Malik, Pieremanuele Canepa, Gopalakrishnan Sai Gautam, Miao Liu, Anubhav Jain, Kristin Persson, and Gerbrand Ceder. Materials design rules for multivalent ion mobility in intercalation structures. *Chemistry of Materials*, 27(17):6016–6021, 2015.
- [26] Ian D Hosein. The promise of calcium batteries: open perspectives and fair comparisons. *ACS Energy Letters*, 6(4):1560–1565, 2021.
- [27] Paul Alexis Chando, Sihe Chen, Jacob Matthew Shellhamer, Elizabeth Wall, Xinlu Wang, Robson Schuarca, Manuel Smeu, and Ian Dean Hosein. Exploring calcium manganese oxide as a promising cathode material for calcium-ion batteries. *Chemistry of Materials*, 35(20):8371–8381, 2023.
- [28] Boosik Jeon, Hunho H Kwak, and Seung-Tae Hong. Bilayered ca0. 28v2o5· h2o: High-capacity cathode material for rechargeable ca-ion batteries and its charge storage mechanism. *Chemistry of Materials*, 34(4):1491–1498, 2022.

- [29] Chong-Yu Du, Zhe Qian, Xun-Lu Li, Jie Zeng, Rui-Jie Luo, Zhe Mei, Zi-Ting Zhou, and Yong-Ning Zhou. Recent progress in cathode materials for ca-ion batteries. *Advanced Materials*, page e10291, 2025.
- [30] Rosalind J Gummow, George Vamvounis, M Bobby Kannan, and Yinghe He. Calcium-ion batteries: current state-of-the-art and future perspectives. *Advanced Materials*, 30(39):1801702, 2018.
- [31] Gopalakrishnan Sai Gautam, Pieremanuele Canepa, Rahul Malik, Miao Liu, Kristin Persson, and Gerbrand Ceder. First-principles evaluation of multi-valent cation insertion into orthorhombic v_2o_5 . *Chemical communications*, 51(71):13619–13622, 2015.
- [32] Xiao Zhang, Xiaoming Xu, Bo Song, Manyi Duan, Jiashen Meng, Xuanpeng Wang, Zhitong Xiao, Lin Xu, and Liqiang Mai. Towards a stable layered vanadium oxide cathode for high-capacity calcium batteries. *Small*, 18(43):2107174, 2022.
- [33] Samuel Jayaraj Richard Prabakar, Amol Bhairuba Ikhe, Woon-Bae Park, Docheon Ahn, Kee-Sun Sohn, and Myoungcho Pyo. Ultra-high capacity and cyclability of β -phase $ca_{0.14}v_2o_5$ as a promising cathode in calcium-ion batteries. *Advanced Functional Materials*, 33(29):2301399, 2023.
- [34] Xiaoming Xu, Manyi Duan, Yunfan Yue, Qi Li, Xiao Zhang, Lu Wu, Peijie Wu, Bo Song, and Liqiang Mai. Bilayered $mg_{0.25}v_2o_5 \cdot h_2o$ as a stable cathode for rechargeable ca-ion batteries. *ACS Energy Letters*, 4(6):1328–1335, 2019.
- [35] Wang Lu, Juefan Wang, Gopalakrishnan Sai Gautam, and Pieremanuele Canepa. Searching ternary oxides and chalcogenides as positive electrodes for calcium batteries. *Chemistry of Materials*, 33(14):5809–5821, 2021.
- [36] Ashley P Black, Carlos Frontera, Arturo Torres, Miguel Recio-Poo, Patrick Rozier, Juan D Forero-Saboya, François Fauth, Esteban Urones-Garrote, M Elena Arroyo-de Dompablo, and M Rosa Palacín. Elucidation of the redox activity of $ca_2mno_3.5$ and ca_2vo_4 in calcium batteries using operando xrd: charge compensation mechanism and reversibility. *Energy Storage Materials*, 47:354–364, 2022.
- [37] Marta Cabello, Francisco Nacimiento, Ricardo Alcántara, Pedro Lavela, Carlos Perez Vicente, and José L Tirado. Applicability of molybdate as an electrode material in calcium batteries: a structural study of layer-type ca_xmoo_3 . *Chemistry of Materials*, 30(17):5853–5861, 2018.
- [38] Tomohiro Tojo, Hayato Tawa, Noriyuki Oshida, Ryoji Inada, and Yoji Sakurai. Electrochemical characterization of a layered α - moo_3 as a new cathode material for calcium ion batteries. *Journal of Electroanalytical Chemistry*, 825:51–56, 2018.
- [39] Munseok S Chae, Hunho H Kwak, and Seung-Tae Hong. Calcium molybdenum bronze as a stable high-capacity cathode material for calcium-ion batteries. *ACS Applied Energy Materials*, 3(6):5107–5112, 2020.
- [40] Thuan Ngoc Vo, Hyeongwoo Kim, Jaehyun Hur, Wonchang Choi, and Il Tae Kim. Surfactant-assisted ammonium vanadium oxide as a superior cathode for calcium-ion batteries. *Journal of materials chemistry A*, 6(45):22645–22654, 2018.

- [41] Marta Cabello, Francisco Nacimiento, José R González, Gregorio Ortiz, Ricardo Alcántara, Pedro Lavela, Carlos Pérez-Vicente, and José L Tirado. Advancing towards a veritable calcium-ion battery: Caco₂ positive electrode material. *Electrochemistry Communications*, 67:59–64, 2016.
- [42] Haesun Park, Christopher J Bartel, Gerbrand Ceder, and Peter Zapol. Layered transition metal oxides as ca intercalation cathodes: A systematic first-principles evaluation. *Advanced Energy Materials*, 11(48):2101698, 2021.
- [43] Junjun Wang, Jianxiang Wang, Yalong Jiang, Fangyu Xiong, Shuangshuang Tan, Fan Qiao, Jinghui Chen, Qinyou An, and Liqiang Mai. Cav₆o₁₆·2.8 h₂o with ca²⁺ pillar and water lubrication as a high-rate and long-life cathode material for ca-ion batteries. *Advanced Functional Materials*, 32(25):2113030, 2022.
- [44] Manuel Smeu, Md Sazzad Hossain, Zi Wang, Vladimir Timoshevskii, Kirk H Bevan, and Karim Zaghib. Theoretical investigation of chevrel phase materials for cathodes accommodating ca²⁺ ions. *Journal of Power Sources*, 306:431–436, 2016.
- [45] Neal Kuperman, Prasanna Padigi, Gary Goncher, David Evans, Joseph Thiebes, and Raj Solanki. High performance prussian blue cathode for nonaqueous ca-ion intercalation battery. *Journal of Power Sources*, 342:414–418, 2017.
- [46] Tomohiro Tojo, Yosuke Sugiura, Ryoji Inada, and Yoji Sakurai. Reversible calcium ion batteries using a dehydrated prussian blue analogue cathode. *Electrochimica Acta*, 207:22–27, 2016.
- [47] Tohru Shiga, Hiroki Kondo, Yuichi Kato, and Masae Inoue. Insertion of calcium ion into prussian blue analogue in nonaqueous solutions and its application to a rechargeable battery with dual carriers. *The Journal of Physical Chemistry C*, 119(50):27946–27953, 2015.
- [48] Prasanna Padigi, Gary Goncher, David Evans, and Raj Solanki. Potassium barium hexacyanoferrate—a potential cathode material for rechargeable calcium ion batteries. *Journal of Power Sources*, 273:460–464, 2015.
- [49] Albert L Lipson, Baofei Pan, Saul H Lapidus, Chen Liao, John T Vaughey, and Brian J Ingram. Rechargeable ca-ion batteries: a new energy storage system. *Chemistry of Materials*, 27(24):8442–8447, 2015.
- [50] Albert L Lipson, Soojeong Kim, Baofei Pan, Chen Liao, Timothy T Fister, and Brian J Ingram. Calcium intercalation into layered fluorinated sodium iron phosphate. *Journal of Power Sources*, 369:133–137, 2017.
- [51] Sanghyeon Kim, Liang Yin, Myeong Hwan Lee, Prakash Parajuli, Lauren Blanc, Timothy T. Fister, Haesun Park, Bob Jin Kwon, Brian J. Ingram, Peter Zapol, Robert F. Klie, Kisuk Kang, Linda F. Nazar, Saul H. Lapidus, and John T. Vaughey. High-voltage phosphate cathodes for rechargeable ca-ion batteries. *ACS Energy Letters*, 5(10):3203–3211, 10 2020.
- [52] Boosik Jeon, Jongwook W. Heo, Joeeun Hyoung, Hunho H. Kwak, Dongmin M. Lee, and Seung-Tae Hong. Reversible calcium-ion insertion in nasicon-type nav₂(po₄)₃. *Chemistry of Materials*, 32(20):8772–8780, 10 2020.

- [53] Zheng-Long Xu, JooHa Park, Jian Wang, Hyunseok Moon, Gabin Yoon, Jongwoo Lim, Yoon-Joo Ko, Sung-Pyo Cho, Sang-Young Lee, and Kisuk Kang. A new high-voltage calcium intercalation host for ultra-stable and high-power calcium rechargeable batteries. *Nature communications*, 12(1):3369, 2021.
- [54] Dereje Bekele Tekliye, Ankit Kumar, Xie Weihang, Thelakkattu Devassy Mercy, Pieremanuele Canepa, and Gopalakrishnan Sai Gautam. Exploration of nasicon frameworks as calcium-ion battery electrodes. *Chemistry of Materials*, 34(22):10133–10143, 2022.
- [55] Dereje Bekele Tekliye and Gopalakrishnan Sai Gautam. Fluoride frameworks as potential calcium battery cathodes. *Journal of Materials Chemistry A*, 12(30):18993–19007, 2024.
- [56] Pierre Hohenberg and Walter Kohn. Inhomogeneous electron gas. *Physical review*, 136(3B):B864, 1964.
- [57] Walter Kohn and Lu Jeu Sham. Self-consistent equations including exchange and correlation effects. *Physical review*, 140(4A):A1133, 1965.
- [58] Lauren E. Blanc, Yunyeong Choi, Abhinandan Shyamsunder, Baris Key, Saul H. Lapidus, Chang Li, Liang Yin, Xiang Li, Bharat Gwalani, Yihan Xiao, Christopher J. Bartel, Gerbrand Ceder, and Linda F. Nazar. Phase stability and kinetics of topotactic dual $\text{Ca}^{2+}\text{-Na}^{+}$ ion electrochemistry in nasicon $\text{Na}_2\text{(PO}_4\text{)}_3$. *Chemistry of Materials*, 35(2):468–481, 2023.
- [59] RD T Shannon and C Tfc Prewitt. Effective ionic radii in oxides and fluorides. *Acta Crystallographica Section B: Structural Crystallography and Crystal Chemistry*, 25(5):925–946, 1969.
- [60] Robert D Shannon. Revised effective ionic radii and systematic studies of interatomic distances in halides and chalcogenides. *Acta crystallographica section A: crystal physics, diffraction, theoretical and general crystallography*, 32(5):751–767, 1976.
- [61] Dereje Bekele Tekliye and Gopalakrishnan Sai Gautam. Accuracy of metagga functionals in describing transition metal fluorides. *Physical Review Materials*, 8(9):093801, 2024.
- [62] Witold Brostow, Jean-Pierre Dussault, and Bennett L Fox. Construction of voronoi polyhedra. *Journal of Computational Physics*, 29(1):81–92, 1978.
- [63] Ilyes Batatia, David P Kovacs, Gregor Simm, Christoph Ortner, and Gábor Csányi. Mace: Higher order equivariant message passing neural networks for fast and accurate force fields. *Advances in neural information processing systems*, 35:11423–11436, 2022.
- [64] Ilyes Batatia, Philipp Benner, Yuan Chiang, Alin M Elena, Dávid P Kovács, Janosh Riebesell, Xavier R Advincula, Mark Asta, Matthew Avaylon, William J Baldwin, et al. A foundation model for atomistic materials chemistry. *The Journal of chemical physics*, 163(18), 2025.
- [65] Oliver T Unke, Stefan Chmiela, Huziel E Saucedo, Michael Gastegger, Igor Poltavsky, Kristof T Schutt, Alexandre Tkatchenko, and Klaus-Robert Muller. Machine learning force fields. *Chemical reviews*, 121(16):10142–10186, 2021.
- [66] Junyoung Choi, Gunwook Nam, Jaesik Choi, and Yousung Jung. A perspective on foundation models in chemistry. *JACS Au*, 5(4):1499–1518, 2025.

- [67] Junfan Xia, Yaolong Zhang, and Bin Jiang. The evolution of machine learning potentials for molecules, reactions and materials. *Chemical Society Reviews*, 54(10):4790–4821, 2025.
- [68] Ilyes Batatia, Simon Batzner, Dávid Péter Kovács, Albert Musaelian, Gregor NC Simm, Ralf Drautz, Christoph Ortner, Boris Kozinsky, and Gábor Csányi. The design space of e (3)-equivariant atom-centred interatomic potentials. *Nature Machine Intelligence*, 7(1):56–67, 2025.
- [69] Mark Neumann, James Gin, Benjamin Rhodes, Steven Bennett, Zhiyi Li, Hitarth Choubisa, Arthur Hussey, and Jonathan Godwin. Orb: A fast, scalable neural network potential. *arXiv preprint arXiv:2410.22570*, 2024.
- [70] Benjamin Rhodes, Sander Vandenhaute, Vaidotas Šimkus, James Gin, Jonathan Godwin, Tim Duignan, and Mark Neumann. Orb-v3: atomistic simulation at scale. *arXiv preprint arXiv:2504.06231*, 2025.
- [71] Matthew K Horton, Patrick Huck, Ruo Xi Yang, Jason M Munro, Shyam Dwaraknath, Alex M Ganose, Ryan S Kingsbury, Mingjian Wen, Jimmy X Shen, Tyler S Mathis, et al. Accelerated data-driven materials science with the materials project. *Nature Materials*, 24(10):1522–1532, 2025.
- [72] Bowen Deng, Peichen Zhong, KyuJung Jun, Janosh Riebesell, Kevin Han, Christopher J Bartel, and Gerbrand Ceder. Chgnet as a pretrained universal neural network potential for charge-informed atomistic modelling. *Nature Machine Intelligence*, 5(9):1031–1041, 2023.
- [73] Gavin Winter and Rafael Gómez-Bombarelli. Simulations with machine learning potentials identify the ion conduction mechanism mediating non-arrhenius behavior in lgps. *Journal of Physics: Energy*, 5(2):024004, 2023.
- [74] Marco Bertani and Alfonso Pedone. Atomic structure of na4p2s7 glass solid electrolyte: Fine-tuning machine learning potentials for enhanced accuracy. *The Journal of Physical Chemistry C*, 129(28):12697–12709, 2025.
- [75] Yanhao Deng, Yan Li, Gopalakrishnan Sai Gautam, Bonan Zhu, and Zeyu Deng. Accelerating the discovery of disordered multi-component solid-state electrolytes using machine learning interatomic potentials. *Journal of Materials Chemistry A*, 13(40):34507–34518, 2025.
- [76] Achintha Krishna Bheemaguli, Penghao Xiao, and Gopalakrishnan Sai Gautam. Evaluation of foundational machine learned interatomic potentials for migration barrier predictions. *Digital Discovery*, 5(4):1809–1819, 2026.
- [77] Yonghyuk Lee, Xiaobo Chen, Sabrina M Gericke, Meng Li, Dmitri N Zakharov, Ashley R Head, Judith C Yang, and Anastassia N Alexandrova. Machine-learning-driven exploration of surface reconstructions of reduced rutile tio2. *Angewandte Chemie*, 137(26):e202501017, 2025.
- [78] Allison Nicole Arber, Vikram, Felix C Mocanu, and M Saiful Islam. Ion migration and dopant effects in the gamma-cspbi3 perovskite photovoltaic material: Atomistic insights through ab initio and machine learning methods. *Chemistry of Materials*, 37(12):4416–4424, 2025.
- [79] Seán R Kavanagh. Identifying split vacancy defects with machine-learned foundation models and electrostatics. *Journal of Physics: Energy*, 7(4):045002, 2025.

- [80] Miguel A Caro. Machine learning based modeling of disordered elemental semiconductors: understanding the atomic structure of a-si and ac. *Semiconductor Science and Technology*, 38(4):043001, 2023.
- [81] Huiju Lee, Vinay I Hegde, Chris Wolverton, and Yi Xia. Accelerating high-throughput phonon calculations via machine learning universal potentials. *Materials Today Physics*, 53:101688, 2025.
- [82] Claudio Zeni, Robert Pinsler, Daniel Zügner, Andrew Fowler, Matthew Horton, Xiang Fu, Zilong Wang, Aliaksandra Shysheya, Jonathan Crabbé, Shoko Ueda, et al. A generative model for inorganic materials design. *Nature*, 639(8055):624–632, 2025.
- [83] Vijay Choyal, Debsundar Dey, and Gopalakrishnan Sai Gautam. Exploration of amorphous v2o5 as cathode for magnesium batteries. *Small*, 21(45):e05851, 2025.
- [84] Aqshat Seth, Rutvij Pankaj Kulkarni, and Gopalakrishnan Sai Gautam. Investigating ionic diffusivity in amorphous lipon using machine-learned interatomic potentials. *ACS Materials Au*, 5(3):458–468, 2025.
- [85] Mariette Hellenbrandt. The inorganic crystal structure database (ICSD)—present and future. *Cystallography Reviews*, 10(1):17–22, 2004.
- [86] Reshma Devi, Keith T Butler, and Gopalakrishnan Sai Gautam. Optimal pre-train/fine-tune strategies for accurate material property predictions. *npj Computational Materials*, 10(1):300, 2024.
- [87] Reshma Devi, Avaneesh Balasubramanian, Keith T Butler, and Gopalakrishnan Sai Gautam. A literature-derived dataset of migration barriers for quantifying ionic transport in battery materials. *Scientific Data*, 12(1):1922, 2025.
- [88] Reshma Devi, Keith T Butler, and Gopalakrishnan Sai Gautam. Leveraging transfer learning for accurate estimation of ionic migration barriers in solids. *npj Computational Materials*, 2026.
- [89] Graeme Henkelman and Hannes Jónsson. Improved tangent estimate in the nudged elastic band method for finding minimum energy paths and saddle points. *The Journal of chemical physics*, 113(22):9978–9985, 2000.
- [90] Daniel Sheppard, Rye Terrell, and Graeme Henkelman. Optimization methods for finding minimum energy paths. *The Journal of chemical physics*, 128(13), 2008.
- [91] Shyue Ping Ong, William Davidson Richards, Anubhav Jain, Geoffroy Hautier, Michael Kocher, Shreyas Cholia, Dan Gunter, Vincent L Chevrier, Kristin A Persson, and Gerbrand Ceder. Python materials genomics (pymatgen): A robust, open-source python library for materials analysis. *Computational Materials Science*, 68:314–319, 2013.
- [92] Norman Neill Greenwood and Alan Earnshaw. *Chemistry of the Elements*. Elsevier, 2012.
- [93] Sambhaji S Shinde, Nayantara K Wagh, Sung-Hae Kim, and Jung-Ho Lee. Li, na, k, mg, zn, al, and ca anode interface chemistries developed by solid-state electrolytes. *Advanced Science*, 10(32):2304235, 2023.

- [94] Tiezhu Xu, Di Wang, Zhiwei Li, Ziyang Chen, Jinhui Zhang, Tingsong Hu, Xiaogang Zhang, and Laifa Shen. Electrochemical proton storage: from fundamental understanding to materials to devices. *Nano-Micro Letters*, 14(1):126, 2022.
- [95] Sicheng Wu, Haocheng Guo, and Chuan Zhao. Challenges and opportunities for proton batteries: From electrodes, electrolytes to full-cell applications. *Advanced Functional Materials*, 34(40):2405401, 2024.
- [96] Ask Hjorth Larsen, Jens Jørgen Mortensen, Jakob Blomqvist, Ivano E Castelli, Rune Christensen, Marcin Dułak, Jesper Friis, Michael N Groves, Bjørk Hammer, Cory Hargus, et al. The atomic simulation environment—a python library for working with atoms. *Journal of Physics: Condensed Matter*, 29(27):273002, 2017.
- [97] Anubhav Jain, Geoffroy Hautier, Shyue Ping Ong, Charles J Moore, Christopher C Fischer, Kristin A Persson, and Gerbrand Ceder. Formation enthalpies by mixing gga and gga+ u calculations. *Physical Review B—Condensed Matter and Materials Physics*, 84(4):045115, 2011.
- [98] Amanda Wang, Ryan Kingsbury, Matthew McDermott, Matthew Horton, Anubhav Jain, Shyue Ping Ong, Shyam Dwaraknath, and Kristin A Persson. A framework for quantifying uncertainty in dft energy corrections. *Scientific reports*, 11(1):15496, 2021.
- [99] Wenhao Sun, Stephen T Dacek, Shyue Ping Ong, Geoffroy Hautier, Anubhav Jain, William D Richards, Anthony C Gamst, Kristin A Persson, and Gerbrand Ceder. The thermodynamic scale of inorganic crystalline metastability. *Science advances*, 2(11):e1600225, 2016.
- [100] MK Aydinol, AF Kohan, Gerbrand Ceder, Kang Cho, and JJPRB Joannopoulos. Ab initio study of lithium intercalation in metal oxides and metal dichalcogenides. *Physical Review B*, 56(3):1354, 1997.
- [101] Charles George Broyden. The convergence of a class of double-rank minimization algorithms 1. general considerations. *IMA Journal of Applied Mathematics*, 6(1):76–90, 1970.
- [102] Søren Smidstrup, Andreas Pedersen, Kurt Stokbro, and Hannes Jónsson. Improved initial guess for minimum energy path calculations. *The Journal of chemical physics*, 140(21), 2014.
- [103] Kamal Choudhary and Brian DeCost. Atomistic line graph neural network for improved materials property predictions. *npj Computational Materials*, 7(1):185, 2021.
- [104] Georg Kresse and Jürgen Hafner. Ab initio molecular dynamics for liquid metals. *Physical review B*, 47(1):558, 1993.
- [105] Georg Kresse and Jürgen Furthmüller. Efficient iterative schemes for ab initio total-energy calculations using a plane-wave basis set. *Physical Review B*, 54(16):11169, 1996.
- [106] John P Perdew, Kieron Burke, and Matthias Ernzerhof. Generalized gradient approximation made simple. *Physical review letters*, 77(18):3865, 1996.
- [107] Reshma Devi, Baltej Singh, Pieremanuele Canepa, and Gopalakrishnan Sai Gautam. Effect of exchange-correlation functionals on the estimation of migration barriers in battery materials. *npj Computational Materials*, 8(1):160, 2022.

- [108] Georg Kresse and Daniel Joubert. From ultrasoft pseudopotentials to the projector augmented-wave method. *Physical Review B*, 59(3):1758, 1999.
- [109] Peter E Blöchl, Ove Jepsen, and Ole Krogh Andersen. Improved tetrahedron method for brillouin-zone integrations. *Physical Review B*, 49(23):16223, 1994.
- [110] Hendrik J Monkhorst and James D Pack. Special points for brillouin-zone integrations. *Physical Review B*, 13(12):5188, 1976.
- [111] Gopalakrishnan Sai Gautam, Ellen B Stechel, and Emily A Carter. Exploring ca-ce-m-o (m= 3d transition metal) oxide perovskites for solar thermochemical applications. *Chemistry of Materials*, 32(23):9964–9982, 2020.
- [112] Bowen Deng, Yunyeong Choi, Peichen Zhong, Janosh Riebesell, Shashwat Anand, Zhuohan Li, Kyu-Jung Jun, Kristin A Persson, and Gerbrand Ceder. Systematic softening in universal machine learning interatomic potentials. *npj Computational Materials*, 11(1):9, 2025.
- [113] Amil Merchant, Simon Batzner, Samuel S Schoenholz, Muratahan Aykol, Gowoon Cheon, and Ekin Dogus Cubuk. Scaling deep learning for materials discovery. *Nature*, 624(7990):80–85, 2023.
- [114] Janosh Riebesell, Rhys EA Goodall, Philipp Benner, Yuan Chiang, Bowen Deng, Gerbrand Ceder, Mark Asta, Alpha A Lee, Anubhav Jain, and Kristin A Persson. A framework to evaluate machine learning crystal stability predictions. *nature machine intelligence*, 7(6):836–847, 2025.
- [115] Jimmy-Xuan Shen, Matthew Horton, and Kristin A Persson. A charge-density-based general cation insertion algorithm for generating new li-ion cathode materials. *npj Computational Materials*, 6(1):161, 2020.